

The influence of circumnuclear environment on the radio emission from TDE jets

A. Generozov^{1*}, P. Mimica², B. D. Metzger¹, N. C. Stone¹, D. Giannios³, M. A. Aloy²

¹*Columbia Astrophysics Laboratory, Columbia University, 550 West 120th Street, New York, NY 10027*

²*Departamento de Astronomía y Astrofísica, Universidad de Valencia, E-46100 Burjassot, Spain*

³*Department of Physics and Astronomy, Purdue University, 525 Northwestern Avenue, West Lafayette, IN 47907, USA*

7 November 2016

ABSTRACT

Dozens of stellar tidal disruption events (TDEs) have been identified at optical, UV and X-ray wavelengths. A small fraction of these, most notably *Swift* J1644+57, produce radio synchrotron emission, consistent with a powerful, relativistic jet shocking the surrounding circumnuclear gas. The dearth of similar non-thermal radio emission in the majority of TDEs may imply that powerful jet formation is intrinsically rare, or that the conditions in galactic nuclei are typically unfavorable for producing a detectable signal. Here we explore the latter possibility by constraining the radial profile of the gas density encountered by a TDE jet using a one-dimensional model for the circumnuclear medium which includes mass and energy input from a stellar population. Near the jet Sedov radius of 10^{18} cm, we find gas densities in the range of $n_{18} \sim 0.1\text{--}1000\text{ cm}^{-3}$ across a wide range of plausible star formation histories. Using one- and two-dimensional relativistic hydrodynamical simulations, we calculate the synchrotron radio light curves of TDE jets (as viewed both on and off-axis) across the allowed range of density profiles. We find that bright radio emission would be produced across the plausible range of nuclear gas densities by jets as powerful as *Swift* J1644+57, and we quantify the relationship between the radio luminosity and jet energy. We use existing radio detections and upper limits to constrain the energy distribution of TDE jets. Radio follow up observations several months to several years after the TDE candidate will strongly constrain the energetics of any relativistic flow.

Key words: black holes physics

1 INTRODUCTION

When a star in a galactic nucleus is deflected too close to the central supermassive black hole (BH), it can be torn apart by tidal forces. During this tidal disruption event (TDE), roughly half of the stellar debris remains bound to the BH, while the other half is flung outwards and unbound from the system. The bound material, following a potentially complex process of debris circularization (Kochanek 1994; Guillochon & Ramirez-Ruiz 2013; Hayasaki et al. 2013, 2016; Shiokawa et al. 2015; Bonnerot et al. 2016), accretes onto the BH, creating a luminous flare lasting months to years (Hills 1975; Carter & Luminet 1982; Rees 1988).

Many TDE flares have now been identified at optical/ultraviolet (UV) (Gezari et al. 2008, 2009; van Velzen et al. 2011; Gezari et al. 2012; Arcavi et al. 2014; Chornock et al. 2014; Holoien et al. 2014; Vinkó et al. 2015; Holoien et al. 2016b) and soft X-ray wavelengths (Bade et al. 1996;

Grupe et al. 1999; Komossa & Greiner 1999; Greiner et al. 2000; Esquej et al. 2007; Maksym et al. 2010; Saxton et al. 2012). Beginning with the discovery of *Swift* J1644+57 (hereafter SwJ1644) in 2011, three additional TDEs have been discovered by their hard X-ray emission (Bloom et al. 2011; Levan et al. 2011; Burrows et al. 2011; Zauderer et al. 2011; Cenko et al. 2012; Pasham et al. 2015; Brown et al. 2015). Unlike the optical/UV/soft X-ray flares, these events are characterized by non-thermal emission from a transient relativistic jet beamed along our line of sight, similar to the blazar geometry of active galactic nuclei (AGN). In addition to their highly variable X-ray emission, which likely originates from the base of the jet (see e.g. Bloom et al. 2011; Crumley et al. 2016), these events are characterized by radio synchrotron emission (Berger et al. 2012; Zauderer et al. 2013; Cenko et al. 2012¹). The latter, more slowly evolving, is powered by shocks formed at the interface between the

¹ *Swift* J1112.2 8238 was not promptly followed up in the radio, but subsequent follow-up with ATCA shows radio emission at a

* ag@astro.columbia.edu

jet and surrounding circumnuclear medium (CNM) (Bloom et al. 2011; Giannios & Metzger 2011; Metzger et al. 2012; De Colle et al. 2012; Kumar et al. 2013; Mimica et al. 2015), analogous to the afterglow of a gamma-ray burst.

Although a handful of jetted TDE flares have been observed, the apparent volumetric rate is a very small fraction ($\sim 10^{-5} - 10^{-4}$) of the observed TDE flare rate (e.g., Burrows et al. 2011, Brown et al. 2015), and an even smaller fraction of the theoretically predicted TDE rate (Wang & Merritt 2004; Stone & Metzger 2016). One explanation for this discrepancy is that the majority of TDEs produce powerful jets, but their hard X-ray emission is relativistically beamed into a small angle θ_b by the motion of the jet, making them visible to only a small fraction of observers. However, the inferred beaming fraction $f_b \approx \theta_b^2/2 \sim 10^{-5} - 10^{-4}$ would require $\theta_b \sim 0.01$ and hence a jet with a bulk Lorentz factor of $\Gamma \gtrsim 1/\theta_b \sim 100$, much higher than inferred for AGN jets or by modeling SwJ1644 (Metzger et al. 2012). This scenario would also require an unphysically low jet half opening angle $\theta_j \lesssim 0.01$.

The low detection rate of hard X-ray TDEs may instead indicate that powerful jet production is intrinsically rare, or that the conditions in the surrounding environment are unfavorable for producing bright emission. Jets could be rare if they require, for instance, a highly super-Eddington accretion rate (De Colle et al. 2012), a TDE from a deeply plunging stellar orbit (Metzger & Stone 2016), a TDE in a retrograde and equatorial orbit with respect to the spin of the black hole (Parfrey et al. 2015), or a particularly strong magnetic flux threading the star (Tchekhovskoy et al. 2014; Kelley et al. 2014). Alternatively, jet formation or its X-ray emission could be suppressed if the disk undergoes Lense-Thirring precession due to a misalignment between the angular momentum of the BH and that of the disrupted star (Stone & Loeb 2012). In the latter case, however, even a ‘dirty’ jet could still be generated, which would produce luminous radio emission from CNM interaction.

Bower et al. (2013) and van Velzen et al. (2013) performed radio follow-up of optical/UV and soft X-ray TDE flares on timescales of months to decades after the outburst (see also Arcavi et al. 2014). They detect no radio afterglows definitively associated with the host galaxy of a convincing TDE candidate.² Bower et al. (2013) and van Velzen et al. (2013) use a Sedov blast wave model for the late-time radio emission to conclude that $\lesssim 10\%$ of TDEs produce jetted emission at a level similar to that in SwJ1644. Mimica et al. (2015) use two-dimensional (axisymmetric) hydrodynamical simulations, coupled with synchrotron radiation transport, to model the radio emission from SwJ1644 as a jet viewed on-axis. By extending the same calculation to off-axis view-

much higher level than expected for the galaxy’s UV/emission line luminosities (Andrew Levan, private communication).

² There were radio detections for two ROSAT flares: RX J1420.4+5334 and IC 3599. However, for RX J1420.4+5334 the radio emission was observed in a different galaxy than was originally associated with the flare. IC 3599 has shown multiple outbursts in the recent years, calling into question whether it is a true TDE at all (Campana et al. 2015). The optical transient CSS100217 (see Drake et al. 2011) had a weak radio afterglow, but its peak luminosity is more consistent with a superluminous supernova than a TDE.

ing angles, they showed that, regardless of viewing angle, the majority of thermal TDE flares should have been detected if their jets were as powerful as SwJ1644, which had a total energy of $\sim 5 \times 10^{53}$ erg.

The recent TDE flare ASSASN-14li (Holoien et al. 2016a) was accompanied by transient radio emission, consistent with either a weak relativistic jet (van Velzen et al. 2016) or a sub-relativistic outflow (Alexander et al. 2016; Krolik et al. 2016) of total energy $\sim 10^{48} - 10^{49}$ erg. The 90 Mpc distance of ASSASN-14li, a few times closer than most previous TDE flares, implies that even if other TDEs were accompanied by similar emission, their radio afterglows would fall below existing upper limits. The extreme contrast between the radio emission of SwJ1644 and ASSASN-14li indicates that the energy distribution of TDE jets is very broad.

Previous works (Bower et al. 2013; van Velzen et al. 2013; Mimica et al. 2015) have generally assumed that all TDE jets encounter a similar gaseous environment as SwJ1644. However, the density of the circumnuclear medium (CNM) depends sensitively on the input of mass from stellar winds and the processes responsible for heating the gas (Quataert 2004; Generozov et al. 2015).

The first goal of this paper is to constrain the range of gas densities encountered by jetted TDEs using the semi-analytic model for the CNM (§2) developed in Generozov et al. (2015) (hereafter GSM15). With this information in hand, in §3 we present hydrodynamical simulations of the jet-CNM shock interaction which determine the radio synchrotron emission across the allowed range of gaseous environments, for different jet energies and viewing angles. In §3.4 we show how the dependence of our results for the peak luminosity, and time to radio maximum, on the jet energy and CNM density can be reasonably understood using a simple analytic blast wave model (§3.2, Appendix B), calibrated to the simulation data. Then, using extant radio detections and upper limits, we systematically constrain the energy distribution of TDE jets. One of our primary conclusions is that TDE jets as energetic as SwJ1644 are intrinsically rare, a result with important implications for the physics of jet launching in TDEs and other accretion flows. Our work also lays the groundwork for collecting and employing future, larger samples of TDEs with radio follow-up, to better constrain the shape of the energy distribution. We summarize and conclude in §4.

2 DIVERSITY OF CNM DENSITIES

2.1 Analytic Constraints

Jet radio emission is primarily sensitive to the density of ambient gas near the Sedov radius, r_{sed} , outside of which the jet has swept up a gaseous mass exceeding its own. For a power law gas density profile, $n = n_{18} (r/10^{18} \text{ cm})^{-k}$,

$$r_{\text{sed}} = 10^{18} \text{ cm} \left(\frac{E(3-k)}{4\pi n_{18} m_p c^2 (10^{18} \text{ cm})^3} \right)^{1/(3-k)} \\ \approx 3E_{54}^{1/2} n_{18}^{-1/2} \text{ pc.} \quad (1)$$

where $E = E_{54} 10^{54}$ erg is the isotropic equivalent energy and in the final equality we have taken $k = 1$, typical of our results described later in this section. For a powerful jet

similar to SwJ1644, the deceleration radius is typically of order a parsec, but it can be as small as 10^{16} cm for a weak jet/outflow, such as that in ASASSN-14li.

Although an initially relativistic jet will slow to sub-relativistic speeds at $r \sim r_{\text{sed}}$, significant deceleration already sets in at the deceleration radius (where the jet has swept up a fraction $\sim 1/\Gamma^3$ of its rest mass),

$$r_{\text{dec}} = \frac{r_{\text{sed}}}{\Gamma^{2/(3-k)}}. \quad (2)$$

According to an observer within the opening angle of the jet, the jet reaches the Sedov and deceleration radii, respectively, at times given by

$$t_{\text{sed}} \simeq \frac{r_{\text{sed}}}{c} \approx 10E_{54}^{1/2} n_{18}^{-1/2} \text{year} \quad (3)$$

$$t_{\text{dec}} \simeq \frac{r_{\text{dec}}}{2\Gamma^2 c} = \frac{t_{\text{sed}}}{2\Gamma^{2(4-k)/(3-k)}} = \frac{t_{\text{sed}}}{2\Gamma^3}, \quad (4)$$

where in the final equality we have again taken $k = 1$.

2.1.1 Dynamical Model of CNM

In the absence of large scale inflows, the dominant source of gas in the CNM of quiescent galaxies is winds from stars in the galactic nucleus. We bracket the range of possible nuclear gas densities using a simple steady-state, spherically symmetric, hydrodynamic model including mass and energy injection from stellar winds. The relevant equations are (e.g. [Holzer & Axford 1970](#); [Quataert 2004](#))

$$\frac{\partial \rho}{\partial t} + \frac{1}{r^2} \frac{\partial}{\partial r} (\rho r^2 v) = q \quad (5)$$

$$\rho \left(\frac{\partial v}{\partial t} + v \frac{\partial v}{\partial r} \right) = -\frac{\partial p}{\partial r} - \rho \frac{GM_{\text{enc}}}{r^2} - qv \quad (6)$$

$$\rho T \left(\frac{\partial s}{\partial t} + v \frac{\partial s}{\partial r} \right) = q \left[\frac{v^2}{2} + \frac{\tilde{v}_w^2}{2} - \frac{\gamma_{\text{ad}}}{\gamma_{\text{ad}} - 1} \frac{p}{\rho} \right], \quad (7)$$

where ρ , v , p , and s are the density, velocity, pressure (we assume an ideal gas with a mean molecular weight of 0.62 and adiabatic index $\gamma_{\text{ad}}=5/3$), and specific entropy of the gas, respectively. The enclosed mass $M_{\text{enc}} = M_{\bullet} + M_{\star}$ includes both the black hole mass M_{\bullet} and enclosed stellar mass $M_{\star} \propto \int \rho_{\star} r^2 dr$, where ρ_{\star} is the stellar density. At the radius of the sphere of influence, r_{inf} , the enclosed stellar and black masses are equal, $M_{\star}(r_{\text{inf}}) = M_{\bullet}$. We take $r_{\text{inf}} = 3.5M_{\bullet,7}^{0.6}$ pc (GSM15), where $M_{\bullet,7} = M_{\bullet}/10^7 M_{\odot}$.

The source term q is the mass injection rate per unit volume per unit time. We take $q = \eta \rho_{\star} / t_h$, where η is a dimensionless efficiency parameter that depends on the properties of the stellar population and t_h is the Hubble time. The $\tilde{v}_w^2 = \sigma(r)^2 + v_w^2$ term in the entropy equation is the specific heating rate of the gas per unit volume, where

$$\sigma \approx \sqrt{\frac{3GM_{\bullet}}{(\Gamma+2)r} + \sigma_{\star}^2}, \quad (8)$$

³ This is really the Lorentz factor of the shock (see [Hascoët et al. 2014](#)). For simplicity, we use the Lorentz factor of the ejecta, which leads to a factor of ~ 2 underestimate of the deceleration time.

is the stellar velocity dispersion, which approaches the constant value of σ_{\star} outside of the influence radius. As in GSM15 we have taken $\sigma_{\star} = 190M_{\bullet,7}^{0.2} \text{kms}^{-1}$ (based on the $M_{\bullet} - \sigma$ relation from [McConnell et al. 2011](#))⁴. v_w^2 is the specific heating rate of the gas from other sources including stellar wind kinetic energy, supernovae, and black hole feedback. We take v_w to be independent of radius.

GSM15 present analytic approximations for the densities and temperatures of steady state solutions to equation (7). We apply these results across the physically allowed range of heating (v_w) and mass injection rates (η), and obtain the corresponding range of gas densities.

2.1.2 Stellar density profiles

We assume a broken power law for the stellar density profile, ρ_{\star} , motivated by Hubble measurements of the radial surface brightness profiles for hundreds of nearby early type galaxies ([Lauer et al. 2007](#)). The measured profile is well fit by the so-called ‘‘Nuker’’ law parameterization, i.e. a piece-wise power law that smoothly transitions from an inner power law slope, γ , to an outer power law slope, β , at a break radius, r_b .

Most galaxies have $0 < \gamma < 1$, and are classified into two broad categories: ‘‘core’’ galaxies with $\gamma < 0.3$ and ‘‘cusp’’ galaxies with $\gamma > 0.5$. Assuming spherical symmetry and a constant mass-to-light ratio, the inner stellar profile translates to a stellar density of $\rho_{\star} \propto r^{-1-\gamma} = r^{-\delta}$.

Cusp-like stellar density profiles are the most relevant to TDEs, since as described in [Stone & Metzger \(2016\)](#), a cuspy stellar density profile results in a higher TDE rate per galaxy. We adopt a fiducial value of $\gamma = 0.7$ ($\delta = 1.7$), motivated by the rate-weighted average value of the inner stellar density profile for the galaxies in [Stone & Metzger \(2016\)](#) (their Table C).

2.1.3 Gas density profiles

Given sufficiently strong heating, a one-dimensional steady-state model for the CNM is characterized by an inflow-outflow structure. The velocity passes through zero at the ‘‘stagnation radius’’, r_s . Mass loss from stars interior to the stagnation radius flows inwards, while that outside of r_s is unbound in an outflow from the nucleus. Fig. 1 shows example radial profiles of the steady-state gas density calculated for a core and a cusp stellar density profile. The stagnation radius is marked as a blue dot on each profile.

As long as the heating parameter, v_w , is greater than the stellar velocity dispersion,

$$r_s \simeq f(\delta) \frac{GM_{\bullet}}{v_w^2} \simeq 0.4M_{\bullet,7} v_{500}^{-2} \text{pc}, \quad (9)$$

where $v_{500} \equiv v_w/500 \text{ km s}^{-1}$ and $f(\delta)$ is a constant of order unity, which in the second equality we take equal to its fiducial value of $f(\delta = 1.7) = 2.5$ (see GSM15). The gas density

⁴ This may be of questionable validity for low mass black holes (e.g. [Greene et al. 2010](#); [Kormendy & Ho 2013](#)). Also, several of the black hole masses used in [McConnell et al. \(2011\)](#) were underestimated ([Kormendy & Ho 2013](#)). However, the precise form of the $M_{\bullet} - \sigma$ relationship has minimal impact on our results

at the stagnation radius, $n(r_s)$, is determined by the rate at which stellar winds inject mass interior to it,

$$\dot{M} = \frac{\eta M_*(r_s)}{t_h} \approx 2.8 \times 10^{-6} M_{\bullet,7}^{0.22} \eta_{0.02} \left(\frac{r_s}{\text{pc}}\right)^{1.3} M_{\odot} \text{yr}^{-1}, \quad (10)$$

where $M_*(r_s)$ is the total stellar mass enclosed within the stagnation radius, $\eta_{0.02} = \eta/0.02$ is normalized to a value characteristic of an old stellar population, and the second equality again assumes our fiducial value of $\delta = 1.7$.

The density at the stagnation radius, $n(r_s)$, is estimated by equating the gas injected by stellar winds over a dynamical time at the stagnation radius, $t_{\text{dyn}}(r_s)$, to the gas mass enclosed at this location.

$$\frac{4\pi}{3} r_s^3 m_p n(r_s) \simeq \dot{M} t_{\text{dyn}}(r_s) \quad (11)$$

For $r_s < r_{\text{inf}}$, $t_{\text{dyn}} = (r_s^3/GM_{\bullet})^{1/2}$, while for $r_s > r_{\text{inf}}$, $t_{\text{dyn}} = (r_s/\sigma_*)$. Thus,

$$n(r_s) \simeq \begin{cases} 0.1 \eta_{0.02} M_{\bullet,7}^{-0.28} \left(\frac{r_s}{\text{pc}}\right)^{-0.2} \text{cm}^{-3} & r_s < r_{\text{inf}} \\ 0.1 \eta_{0.02} M_{\bullet,7}^{0.02} \left(\frac{r_s}{\text{pc}}\right)^{-0.7} \text{cm}^{-3} & r_s > r_{\text{inf}}, \end{cases} \quad (12)$$

For sufficiently strong heating, the stagnation radius will lie inside the SMBH's sphere of influence and will be given by equation (9). In this case,

$$n(r_s) \simeq 0.2 v_{500}^{0.4} \eta_{0.02} M_{\bullet,7}^{-0.48} \text{cm}^{-3}, \quad (13)$$

Near the stagnation radius, GSM15 found that the radial gas profile has a power-law slope of $k \approx (4\delta - 1)/6$, which for our fiducial value of $\delta = 1.7$ gives $n \propto r^{-1}$. The gas density steepens towards smaller radii, approaching $n \propto r^{-1.5}$, for radii well inside of both the stagnation radius of the flow and the SMBH's sphere of influence. The gas profile flattens to $n \propto r^{1-\delta}$ between the stagnation radius and the stellar break radius; however, for our fiducial value of $\delta = 1.7$, the resulting profile $n \propto r^{1-\delta} \approx r^{-0.7}$ is only moderately changed. We expect at the deceleration radius of most jets is bracketed by $r^{-0.7}$ and $r^{-1.5}$. For simplicity we adopt

$$n(r) = n_{18} \left(\frac{r}{10^{18} \text{cm}}\right)^{-1}, \quad (14)$$

as our fiducial density profile, where n_{18} is the density at $r = 10^{18}$ cm. We explore the effects of the density slope on jet radio emission in § 3.3

Alexander et al. (2016) use radio observations of the ASSASN-14li flare to infer a nuclear gas density profile of $n \propto r^{-2.6}$ for its host galaxy on scales of $\sim 10^{16}$ cm—much steeper than our fiducial density profile. However, we note that this galaxy was active before the flare, possibly explaining the unusually steep density profile.

Combining equations (12) and (14), we obtain

$$n_{18} \simeq \begin{cases} 0.4 \left(\frac{r_s}{\text{pc}}\right)^{0.8} M_{\bullet,7}^{-0.28} \eta_{0.02} \text{cm}^{-3} & r_s < r_{\text{inf}} \\ 0.4 \left(\frac{r_s}{\text{pc}}\right)^{0.3} M_{\bullet,7}^{0.02} \eta_{0.02} \text{cm}^{-3} & r_s > r_{\text{inf}}. \end{cases} \quad (15)$$

For sufficiently strong heating, the stagnation radius will lie inside the sphere of influence and will be given by equation (9). In this case,

$$n_{18} \simeq 0.2 M_{\bullet,7}^{0.52} v_{500}^{-1.6} \eta_{0.02} \text{cm}^{-3}. \quad (16)$$

As shown in Fig. 1, the gas density profile steepens outside

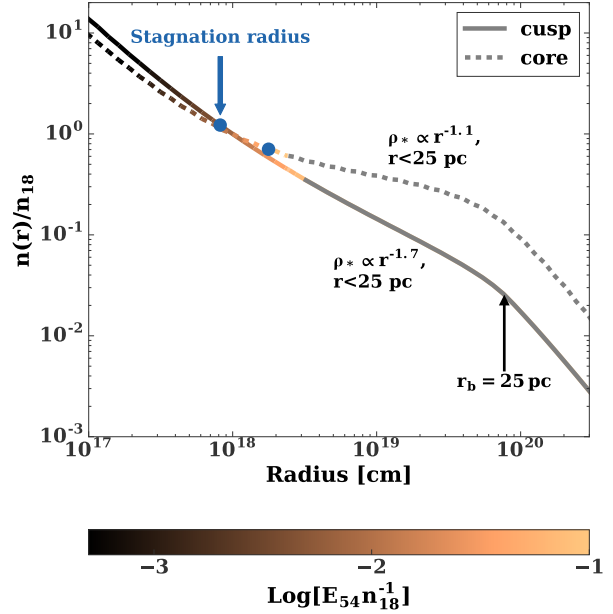


Figure 1. Steady-state radial profiles of the CNM gas density, normalized to its value at 10^{18} cm, n_{18} . The profiles are calculated for a black hole mass of $10^7 M_{\odot}$ and a gas heating parameter of $v_w = 600$ km s $^{-1}$. Cusp and core stellar density profiles are shown with solid and dashed lines, respectively. The line colors denote the ratio of isotropic equivalent jet energy to n_{18} which results in $r = r_{\text{sed}}$ at each radius.

the break radius r_b of the stellar density profile. However, this will only impact the radio emission near its maximum if r_b lies inside of the Sedov radius, r_{sed} (eq. 1). The lines in Fig. 1 are colored according to the combination of jet energy and CNM density n_{18} which results in $r = r_{\text{sed}}$ at each radius. The measured break radii of all but four of the Lauer et al. (2007) galaxies exceed 10 parsecs, which greatly exceeds r_{sed} even in the case of a very energetic jet ($E = 4 \times 10^{54}$ erg) in a low density CNM of $n_{18} \sim 1$ cm $^{-3}$. The presence of a nuclear star cluster (NSC) in the galactic center could produce another break in the stellar density profile near the outer edge of the cluster, which is typically located at $r_{\text{nsc}} \sim 1-5$ pc (Georgiev & Böker 2014). But even in this case, only particular combinations of high E /low n_{18} result in $r_{\text{sed}} > r_{\text{nsc}}$. We therefore neglect the effects of an outer break in the stellar density profile in our analysis.

2.1.4 Allowed Density Range

We now estimate the allowed range in the normalization of the CNM gas profile, n_{18} . We assume that star formation occurs in two bursts, an old burst of age comparable to the Hubble time $t_h = 10^{10}$ yr, and a “young” burst of variable age $t_{\text{burst}} \ll t_h$ which contributes a fraction f_{burst} of the stellar mass. We assume a Salpeter IMF for both stellar populations.

For a sufficiently large burst of age $\lesssim 40$ Myr, gas heating is dominated by the energetic winds of massive stars.⁵

⁵ Core-collapse SNe are also an important heating source. In a young stellar population, the power from core-collapse supernovae

In this case the mass return (η) and heating parameters (v_w) are calculated as described in Appendix C of GSM15. Given $\eta(t_{\text{burst}}, f_{\text{burst}})$ and $v_w(t_{\text{burst}}, f_{\text{burst}})$, we calculate n_{18} following equation (16).

For an older stellar population, a few different sources contribute to gas heating, including Type Ia Supernovae (SNe)⁶ and AGN feedback. We focus on quiescent phases, during which SNe Ia dominate. As discussed in GSM15, SNe Ia clear out the gas external to a critical radius, r_{Ia} , where the interval between successive Ia SNe equals the dynamical (gas inflow) timescale. For an old stellar population, n_{18} is estimated by equating r_{Ia} with the stagnation radius in equation (15). The Ia radius is calculated as described in GSM15 at times $t > 300$ Myr after star formation, and is taken to be constant for $t = 40 - 300$ Myr.⁷

Fig. 2 shows how n_{18} varies with the young starburst properties, f_{burst} and t_{burst} . We find a maximum density of $n_{18} \sim 1,300 M_{\bullet,7}^{0.5} \text{ cm}^{-3}$ is achieved for a burst of age $t_{\text{burst}} \sim 4$ Myr which forms most of the stars in the nucleus ($f_{\text{burst}} \sim 1$). In this case, both the energy and mass budgets of the CNM are dominated by fast winds from massive stars. Although a large gas density is present immediately after a starburst, the density will decline with the wind mass loss rate, approximately $\propto t^{-3}$, i.e. by an order of magnitude within just a few Myr.

By contrast, the lowest allowed density $\sim 0.02 M_{\bullet,7}^{0.5} \text{ cm}^{-3}$ is achieved for a relatively modest burst of young stars $t_{\text{burst}} \approx 10^6$ Myr, which forms a fraction $f_{\text{burst}} = 4 \times 10^{-4}$ of the total stellar mass. In this case the young massive stars provide a high heating rate, while the mass injection rate is comparatively low and receives contributions from both young and old stars.

The lowest allowed n_{18} may be an underestimate as we do not include the effects of discreteness on the assumed stellar population. In particular, we assume that stars provide a spatially homogeneous heating source and mass source, even on small radial scales where the number of massive stars present may be very small. The doubly hatched region in Fig. 2 denotes the region where less than one massive star ($\gtrsim 15 M_{\odot}$) is on average present inside of the nominal stagnation radius (eq. 9). Discreteness effects are thus important for relatively small bursts of star formation, including the case described above which gives the minimum n_{18} . If we instead equate the stagnation radius to the radius enclosing a single star of mass $\gtrsim 15 M_{\odot}$, we find a larger value of $n_{18} \sim 0.3 M_{\bullet,7}^{-0.4} \text{ cm}^{-3}$. The true minimum density therefore likely lies closer to $0.3 M_{\bullet,7}^{-0.4} \text{ cm}^{-3}$. However, we caution that this is a very crude estimate, and the low number of mass and heat sources means could there could be considerable scatter about this value from stochastic varia-

tions in the stellar population. Additionally, stellar angular momentum could reduce the density (see e.g. Cuadra et al. 2006).

Finally, French et al. (2016b) find that most optical/UV⁸ TDEs have evidence of recent star formation. Six of the eight galaxies in their sample are consistent with an exponentially declining star formation history, forming 10% of the stars in the galaxy over $\sim 100 - 200$ Myr⁹. In this region of parameter space corresponding to the right side of Fig. 2, gas heating rate is dominated by SN Ia and $n_{18} \sim 10 \text{ cm}^{-3}$.

In summary, the CNM densities of quiescent galaxies vary from $\min(n_{18}) \sim 0.3 M_{\bullet,7}^{-0.4} \text{ cm}^{-3}$ to $\max(n_{18}) \sim 1.3 \times 10^3 M_{\bullet,7}^{0.5} \text{ cm}^{-3}$, with a characteristic value of $n_{18} \sim 10 \text{ cm}^{-3}$ expected for TDE host galaxies.

2.1.5 Mass drop-out from star formation?

Our CNM model predicts the total gas density as sourced by stellar winds, including both hot and cold phases. For the first few Myr after a starburst, the injected stellar wind material is hot ($T \gtrsim 10^7$ K) due to the thermalized wind kinetic energy. At later times, SNe Ia provide intermittent heating, but the stellar wind material that accumulates on small radial scales between successive SNe Ia may be much cooler, with at most the virial temperature $\sim 2 \times 10^5 M_{\bullet,7}^{0.4}$ K. This means the gas could condense into cold clumps.

The propagation of jets through a medium containing clumps, clouds or stars has been studied in the context of AGNs (e.g., Wang et al. 2000; Choi et al. 2007) and microquasars (e.g., Araudo et al. 2009; Perucho & Bosch-Ramon 2012). It was found that the presence of these obstacles has an effect on the long-term jet stability, as well as observational signatures at high energies. However, the situation is different in the case of either a very wide or ultra-relativistic outflow (such as a GRB) for which the emission is expected to be similar for a clumpy and a smooth medium with the same average density (e.g. Nakar & Granot 2007; van Eerten et al. 2009; Mimica & Giannios 2011). In the case of SwJ1644, the inferred angular width of the jet (especially of the slow component) is much larger than in the case of AGNs and microquasars (see discussion in Mimica et al. 2015). In fact, it is large enough to make the overall effect of the presence of any inhomogeneities in the external medium minor. An analogous effect is found in case of SN remnants sweeping a clumpy medium (Obergaugliger et al. 2015). We note that we call the ‘‘slow component of the jet,’’ may in fact be an unrelated mildly relativistic outflow.

On the other hand, a fraction of the cold gas may also condense into stars. However, once the density of the hot phase is sufficiently reduced, the cooling time will become much longer the dynamical time and the gas will become

exceeds that from massive stellar winds after ~ 6 Myr (Voss et al. 2009). However, due to discreteness effects the heating from massive star winds will be more important on small scales.

⁶ Unbound debris streams from TDEs potentially provide another source of heating localized in the galactic center (Guillochon et al. 2016), which we neglect.

⁷ GSM15 incorrectly extrapolated the Ia rate valid at times $t > 300$ Myr back to a time $t = 3$ Myr, which is unphysical as no white dwarfs would have formed by this time. Although its qualitative impact on our results is minimal, here we instead take the Ia rate to be 0 for $t < 40$ Myr.

⁸ We are not aware of any studies of host galaxy properties for the x-ray selected sample

⁹ While this paper was in press French et al. (2016a) presented a more detailed study of stellar populations of TDE hosts, showing that their recent starbursts are older and smaller than we assume here, reducing the expected n_{18} to $\sim 2 \text{ cm}^{-3}$. However, a larger density could still be possible if the starburst is centrally concentrated, as observed in nearby post-starburst galaxies (Pracy et al. 2012).

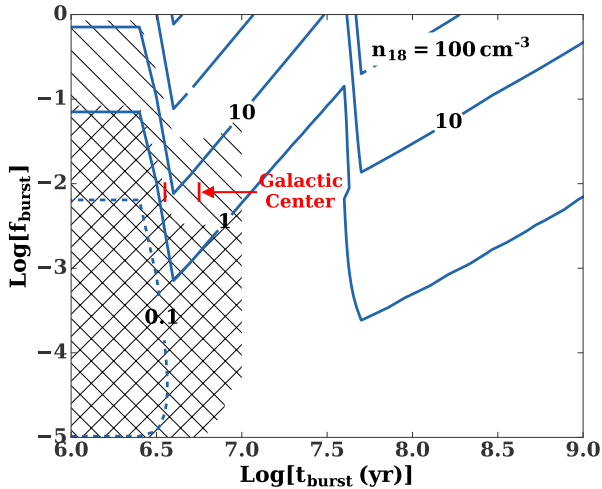


Figure 2. Contours of n_{18} , the CNM density at $r = 10^{18}$ cm (blue lines), as a function of the stellar population in the galactic nucleus. The star formation is parameterized assuming that a fraction f_{burst} of the stars form in a burst of age t_{burst} , while the remaining stars formed a Hubble time ago. We have assumed a black hole mass of $10^7 M_{\odot}$ and that both the young and old stars possess a cusp-like density profile, with a corresponding gas density profile $n \propto r^{-1}$. Hatched areas indicate regions of parameter space where massive stars ($> 15 M_{\odot}$) dominate the gas heating rate, but less than one (doubly hatched) or less than ten (singly hatched) massive stars are present on average inside the nominal stagnation radius (eq. 9). In these regions discreteness effects not captured by our formalism are potentially important. The red line shows the approximate location of the Galactic Center in this parameter space (see text for details).

thermally stable, causing the condensation process to stop. For gas at the virial temperature of $\sim 2 \times 10^5 M_{\bullet,7}^{0.4}$ K, we find that thermal stability would be achieved for $n_{18} \sim 0.6 M_{\bullet,7}^{0.2} \text{ cm}^{-3}$ (where we have defined thermal stability as the cooling time being ten times longer than the dynamical time-scale [McCourt et al. 2012](#)). In fact this estimate is conservative. If a fraction of the gas condenses into stars, then feedback from stellar winds would suppress further fragmentation. More realistically, the CNM density may be reduced by less than a factor of ~ 2 by star formation.

2.1.6 Constraints from the Galactic Center

Due to its close proximity, it is possible to directly observe the gas density distribution on parsec scales in the Galactic Center (GC). [Baganoff et al. \(2003\)](#) find that the hot, diffuse plasma within 10 arcseconds ($\sim 10^{18}$ cm) of Sgr A* has a root mean square electron density of $\sim 26 \text{ cm}^{-3}$.

In Fig. 2 we show two sets of two-burst star formation models which produce heating and mass return parameters comparable to those derived from the full star formation history of the GC from [Pfuhl et al. \(2011\)](#) (their Fig. 14). Our formalism gives values of $n_{18} \sim 3 - 5 \text{ cm}^{-3}$, too low compared to observations. Discrepancy at this level is not surprising because our model is spherically symmetric, while in reality many of the massive stars in the GC are concentrated in two counter-rotating disks ([Genzel et al. 2003](#)) with a possibly top heavy IMF ([Bartko et al. 2010](#); [Lu et al. 2013](#)). The disk stars extend from $\sim 10^{17} - 10^{18}$ cm and

Table 1. Parameters for on-axis jet simulations.

	Fiducial value	Other values
Fast component ($\Gamma = 10$)		
$[\theta_{\min}, \theta_{\max}]$	[0, 0.1] radians	
$E_{\text{ISO}}/10^{54}$ erg	4	0.04, 0.4
$E/10^{54}$ erg	0.02	
Slow component ($\Gamma = 2$)		
$[\theta_{\min}, \theta_{\max}]$	[0.1, $\pi/2$] radians	
$E_{\text{ISO}}/10^{54}$ erg	4.7	0.047, 0.47
$E/10^{54}$ erg	0.47	
Microphysical parameters		
ϵ_e	0.1	
ϵ_b	0.002	
p	2.3	
Nuclear gas density		
n_{18}/cm^{-3}	60	2, 11, 345, 2000

inject $\sim 10^{-3} M_{\odot} \text{ yr}^{-1}$ of stellar wind material, much more than the $\sim 4 \times 10^{-5} M_{\odot} \text{ yr}^{-1}$ expected for the global star formation history, explaining the large density of hot gas.

In short, accurate modeling of the gas distribution in a particular galactic nucleus, requires detailed knowledge of the distribution of stars. Our goal here has been to bracket the range of possible nuclear gas densities, by considering a broad range of stellar populations.

The Galactic Center also contains a cold circumnuclear ring (e.g. [Becklin et al. 1982](#)) with an opening angle of $\sim 12 \pm 3^{\circ}$ ([Lau et al. 2013](#)) and a spatially averaged density of $\sim 10^5 \text{ cm}^{-3}$ (although this varies by a few orders of magnitude throughout the ring—see [Ferrière 2012](#) and references therein). Additionally, the volume from ~ 0.4 – 2.5 pc is filled with warm, ionized atomic gas with density of $\sim 900 \text{ cm}^{-3}$ ([Ferrière 2012](#)). This gas cannot be accounted for in our model, and may originate from larger scale inflows or a disrupted giant molecular cloud.

3 SYNCHROTRON RADIO EMISSION

3.1 Numerical Set-Up

We calculate the synchrotron radio emission from the jet-CNM shock interaction across the physically plausible range of nuclear gas densities. We perform both one- and two-dimensional (axisymmetric) relativistic hydrodynamical simulations using the numerical code MRGENESIS ([Mimica et al. 2009a](#)). MRGENESIS periodically outputs snapshots with the state of the fluid in its numerical grid. These snapshots are then used as an input to the radiative transfer code SPEV ([Mimica et al. 2009b](#)). SPEV detects the forward shock at the jet-CNM interface, accelerates non-thermal electrons behind the shock front, evolves the electron energy and spatial distribution in time, and computes the non-thermal emission taking into account the synchrotron self-absorption (interested readers can find many more technical details in [Mimica et al. 2016](#)). We use the same numerical grid resolution as in [Mimica et al. \(2015\)](#).

For the jet angular structure, we adopt the preferred two-component model for SwJ1644 from [Mimica et al. \(2015\)](#), corresponding to a fast, inner core with Lorentz factor $\Gamma = 10$, surrounded by a slower, $\Gamma = 2$ outer sheath. The ratio of the beaming-corrected energy of the fast component

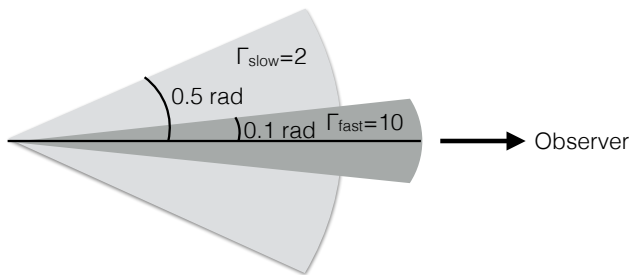


Figure 3. Initial geometry of the jet used for our hydrodynamic simulations. We note that for 1D- two component jet models, we perform separate models for the inner fast core and for the outer sheath, which are later combined to provide the resulting emission. For our 1D simulation we take a slow component extending from $0-\pi/2$ radians to account for the effects of jet spreading.

is fixed to be 4% of that of the slow sheath. A schematic depiction of the jet geometry is shown in Fig. 3. In our 2D simulations the fast inner core spans an angular interval $0 - 0.1$ radians, while the slow outer sheath extends from 0.1 radians to 0.5 rad. The time dependence of the jet kinetic luminosity is given by (Mimica et al. 2015)

$$L_{j,\text{ISO}}(t) = L_{j,0} \max[1, (t/t_0)]^{-5/3}, \quad (17)$$

where $t_0 = 5 \times 10^5$ s is the duration of peak jet power. This is assumed to match that of the period of the most luminous X-ray emission of SwJ1644. Integrating equation (17) from $t = 0$ to ∞ gives the isotropic equivalent energy of the jet, E_{ISO} , where $L_{j,0} = 0.4 E_{\text{ISO}}/t_0$. For the microphysical parameters characterizing the fraction of the post-shock thermal energy placed into relativistic electrons (ϵ_e) and magnetic field (ϵ_B), and the power-law slope of the electron energy distribution p , we adopt the values from the best fit model in Mimica et al. (2015) (see Table 1).

For our 1D simulations, we modify the geometry of the slow sheath to better mimic the results of the 2D simulations. In our 2D models the sheath is injected within a relatively narrow angular interval; however, at late stages of evolution the bow shock created by the jet-CNM interaction spans a much larger angular range due to lateral spreading. To account for the slow component becoming more isotropic near peak emission in our 2D simulations (bottom two panels of Fig. 8 in Mimica et al. 2015), we instead take the slow component to extend from 0.1 to $\pi/2$ radians in our 1D models. We keep the true energy of the slow component fixed so that the isotropic equivalent energy of the slow component is a factor of $[\cos(0.1) - \cos(0.5)]/[\cos(0.1) - \cos(\pi/2)] \approx 0.12$ smaller than in the corresponding 2D simulations.

Figure 4 compares light curves calculated from this modified 1D approach to the results of the full 2D simulations. Despite the slow sheath being initially much broader in the 1D simulations than in 2D, the resulting light curves agree surprisingly well. The agreement is particularly good at the highest densities ($n_{18} = 2000 \text{ cm}^{-3}$) because the slow component rapidly isotropizes in 2D. At lower densities ($n_{18} = 60 \text{ cm}^{-3}$), the agreement with the 1D simulations is not as good, particularly at 30 GHz. At high densities, the jet is quickly isotropized and its morphology is closer to that of the wedge we assume in our 1D model. Hence, the late time evolution of the light curve at high CNM densities

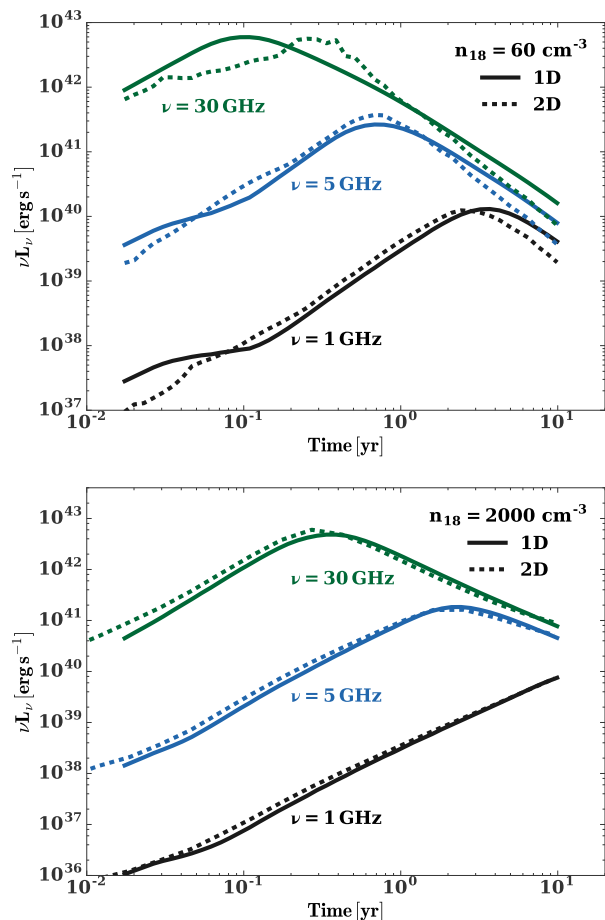


Figure 4. Comparison of light curves from 1D and 2D simulations for an on-axis observer ($\theta_j = 0$). We assume that the gas density $n \propto r^{-1}$.

is well captured by the 1D model. At lower densities, the optically thin emission shows a strongly perturbed axially symmetric jet, with an intricate morphology (Mimica et al. 2015). Thus, the 1D model is not optimal for capturing the slope of the light curve, especially at the highest frequencies (since the ejecta becomes optically thin earlier). However, the 1D model reproduces the peak luminosity from the 2D results within a factor of ~ 2 for $n_{18}=60 \text{ cm}^{-3}$ across all frequencies.

3.2 Analytic Estimates

The dependence of the synchrotron peak luminosity, peak time, and late time luminosity power law slope on the ambient gas density and jet parameters can be estimated analytically using a simple model for the emission from a homogeneous, shocked slab of gas behind a self-similarly expanding blast wave (e.g., Sari et al. 1998; Granot & Sari 2002). The relevant results, as presented by Leventis et al. (2012), are summarized in Appendix B. The peak luminosity of the slow

component of the jet can be estimated from equation (B6),

$$\nu L_{\nu,p} = \begin{cases} 2.7 \times 10^{40} \left(\frac{E}{10^{54} \text{ergs}} \right)^{0.59} \left(\frac{\epsilon_e}{0.1} \right)^{1.3} \times \\ \left(\frac{\epsilon_b}{0.002} \right)^{0.825} \left(\frac{\nu_{\text{obs}}}{5 \text{GHz}} \right)^{0.35} n_{18}^{1.24} \text{erg s}^{-1} & \text{Opt. Thin} \\ 1.1 \times 10^{42} \left(\frac{E}{10^{54} \text{ergs}} \right)^{0.87} \left(\frac{\epsilon_e}{0.1} \right)^{0.61} \times \\ \left(\frac{\epsilon_b}{0.002} \right)^{0.26} \left(\frac{\nu_{\text{obs}}}{5 \text{GHz}} \right)^{2.01} n_{18}^{-0.14} \text{erg s}^{-1} & \text{Opt. Thick,} \end{cases} \quad (18)$$

where we have adopted fiducial values for the power-law slope of the gas density profile, $k = 1$, and the electron energy distribution, $p = 2.3$. The top and bottom lines apply, respectively, to the shocked CNM being optically thin and optically thick at the deceleration time (as delineated by blue lines in Fig. 5).

The peak luminosity in the optically thin case depends sensitively on n_{18} , while in the optically thick regime the dependence on density is much weaker. The peak fluxes in equation (18) are normalized to match those derived from our numerical results.

The time of maximum flux, for the same fiducial values ($k = 1$, $p = 2.3$), is given by equation (B3),

$$t_p = \begin{cases} 500 E_{54}^{0.5} n_{18}^{-0.5} \text{ days} & \text{Opt. Thin} \\ 50 \left(\frac{E}{10^{54} \text{ergs}} \right)^{0.32} \left(\frac{\epsilon_e}{0.1} \right)^{0.45} \left(\frac{\epsilon_b}{0.002} \right)^{0.37} \\ \left(\frac{\nu_{\text{obs}}}{5 \text{GHz}} \right)^{-1.1} n_{18}^{0.4} \text{ days} & \text{Opt. Thick,} \end{cases} \quad (19)$$

where again the normalizations are chosen to match our numerical results. Note that for the optically thin case the peak time is within a factor of two of the deceleration time (eq. 4).

In general, more energetic jets produce emission which peaks later in time. However, the scaling of t_p with n_{18} is more complicated: if the emitting region is optically thick at the deceleration time, then the peak time increases with CNM density. In this case the peak flux occurs when the self-absorption frequency passes through the observing band, and this happens later if the nuclear gas density is higher. Otherwise, peak flux is achieved near the deceleration time, which is a decreasing function of n_{18} (eq. 4). Fig. 5 shows the division between the optically-thick and optically-thin regimes at 1 and 30 GHz in the parameter space of jet energy and n_{18} .

3.3 Numerical Light Curves

As summarized in Table 1 (and shown in Fig 5), we calculate light curves for a grid of on-axis jet simulations for five different values of n_{18} (2, 11, 60, 345, and 2000 cm^{-3}) and three different values of the (beaming-corrected) jet energy E (5×10^{51} , 5×10^{52} , 5×10^{53} erg).

The left panels of Fig. 6 show example light curves for

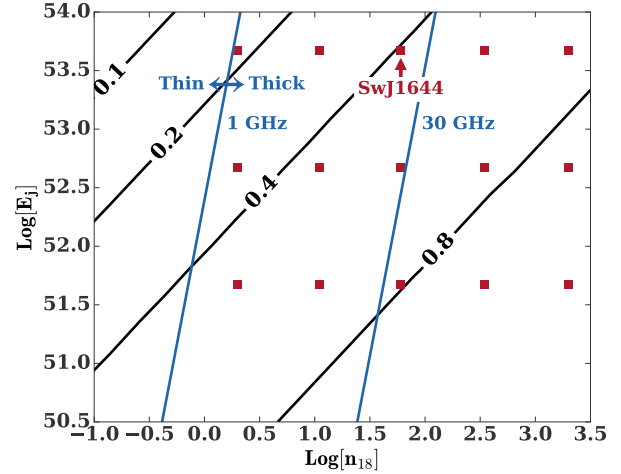


Figure 5. Contours of the fraction of the kinetic energy of the slow component of the jet ($\Gamma = 2$) which is dissipated at the reverse shock in the parameter space of jet energy, E_j , and CNM density, n_{18} . The parameters of the suite of jet simulations presented in this paper are shown as red squares. The approximate location of SwJ1644 in the parameter space is also labeled. Blue lines delineate the parameter space where the slow component of the jet is optically thin/thick at the deceleration time at 1 GHz (left line) and 30 GHz (right line).

different jet energies and nuclear gas densities. The peak luminosity is roughly linearly proportional to the jet energy and is virtually independent of the ambient density. For high CNM densities and low frequencies this is to be expected because the emission is dominated by the slow component, which is optically thick at the deceleration time. However, for high frequencies and small CNM densities, the peak luminosity of the slow component falls off, as shown by the lighter shaded lines in the right panels of Fig. 6. Coincidentally, the fast component just compensates for this decline, resulting in the total (fast + slow) on-axis peak luminosity being weakly dependent on n_{18} across the entire parameter space. A good approximation to this universal peak luminosity is given by equation 18 for $n_{18} = 2000 \text{ cm}^{-3}$ in the optically-thick case.

Fig. 6 also makes clear that the peak time increases with the ambient gas density. Across most of the parameter space the peak occurs after the deceleration time, when the emitting region transitions from optically thick to optically thin, as occurs later for larger n_{18} . However, at high frequencies and low densities the slow component is optically thin at the deceleration time, and thus its peak time is a decreasing function of n_{18} . For example, at 30 GHz, the slow component peaks later for $n_{18} = 2 \text{ cm}^{-3}$ than for $n_{18} = 60 \text{ cm}^{-3}$.

The numerical light curves are well fit by a broken power law (see e.g. Leventis et al. 2012),

$$L_{\nu}(t) = \frac{L_{\nu,p}}{2^{-1/s}} \left[\left(\frac{t}{t_p} \right)^{-sa_1} + \left(\frac{t}{t_p} \right)^{-sa_2} \right]^{-1/s}, \quad (20)$$

where $L_{\nu,p}$ and t_p are the peak luminosity and time given by equations (18) and (19), respectively. The parameter s controls the sharpness of the transition between the early-time power-law slope a_1 and the late-time slope a_2 . Fitting to the numerical light curves, we find that $s \sim 1.0$, $a_1 \sim$

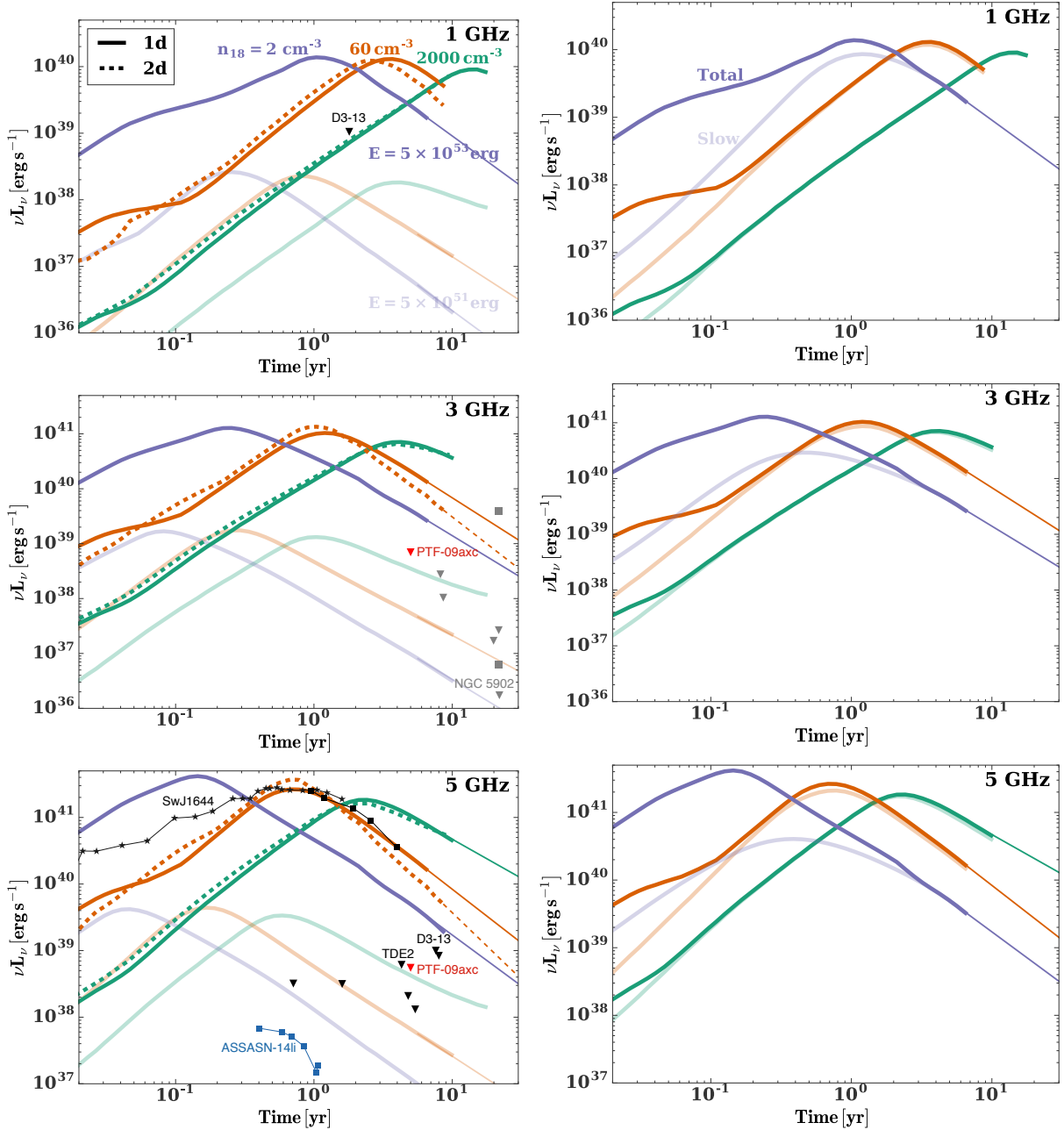
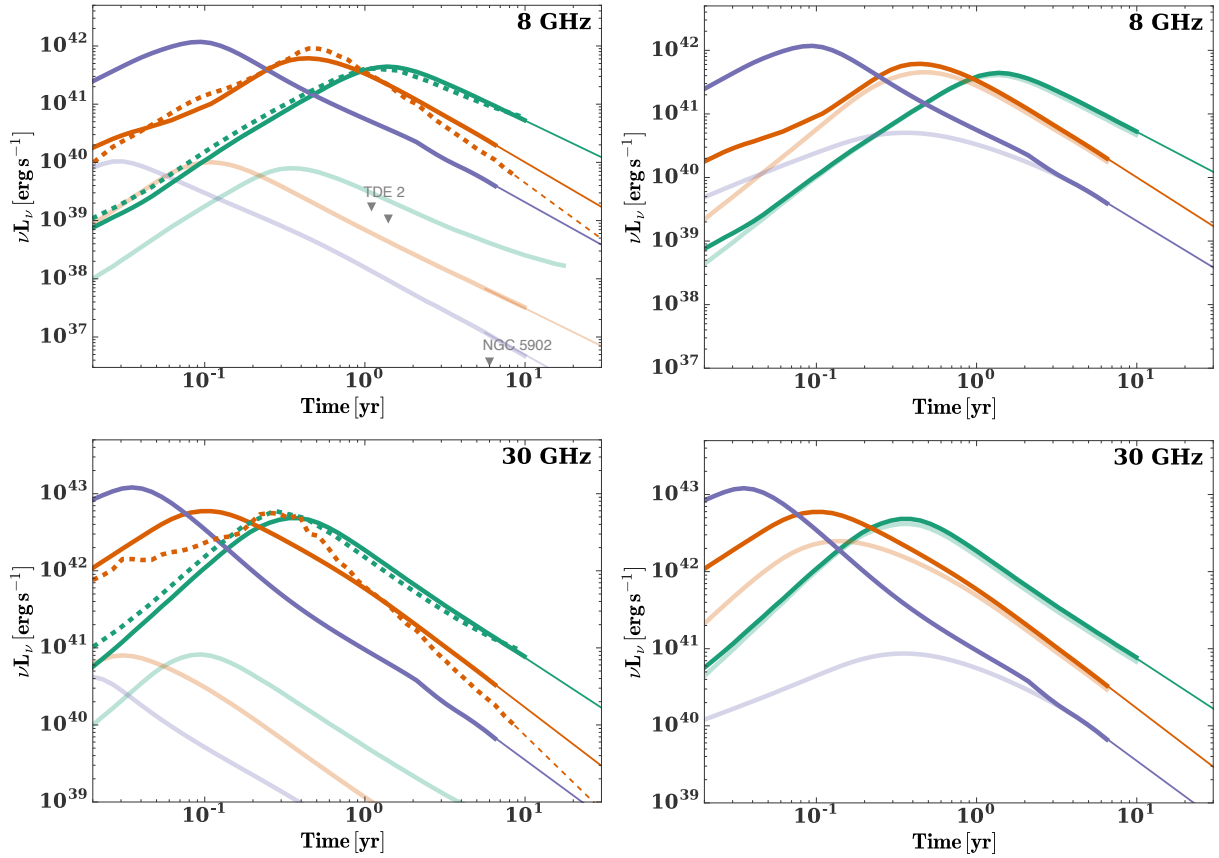


Figure 6. *Left:* Radio light curves as viewed on axis ($\theta_{\text{obs}} = 0$) for jet energies of 5×10^{53} erg (*darker-shaded lines*) and 5×10^{51} erg (*lighter-shaded lines*), for values of $n_{18} = 2$ (blue), 60 (red), and 2000 (green) cm^{-3} . Solid lines show the result of 1D simulations, while 2D light curves are shown as dashed lines (when available). Thick lines show the results of our numerical calculation, while thin lines are power law extrapolations. A gas density profile of $n \propto r^{-1}$ is used for all of the light curves. Radio upper limits and detections are shown as triangles and squares, respectively. The single upper limit in the top panel is for D3-13 at 1.4 GHz from Bower (2011a). Gray triangles and squares in the second panel indicate upper limits and detections at 3.0 GHz from Bower et al. (2013), while the red triangle is the 3.5 GHz upper limit for PTF-09axc from Arcavi et al. (2014). Black triangles in the third panel indicate upper limits at 5.0 GHz from van Velzen et al. (2013). The red triangle shows the 6.1 GHz upper limit for PTF-09axc from Arcavi et al. (2014). The connected black stars show early time data for SwJ1644 taken with EVLA (Berger et al. 2012; Zauderer et al. 2013), while the connected black squares show late time measurement with the European VLBI network (Yang et al. 2016). Connected blue squares show 5 GHz data for ASSASN-14li (Alexander et al. 2016). Note that we have subtracted the observed quiescent radio emission for ASSASN-14li). We have labeled events which have upper limits across multiple frequencies *Right:* 5×10^{53} erg on-axis light curves from left column (*darker-shaded lines*) and corresponding slow component light curves (*lighter-shaded lines*). Figure is continued on next page.

Figure 6 – *continued* Simulation results at 8 and 30 GHz. Top left panel includes 8.4 GHz and 7.9 GHz upper limits for TDE2 and SDSSJ1201+30 respectively (see Table 2)



1.7, and $a_2 \sim -1.4$, the latter approximately agreeing with the analytic estimate in equation (B7). These parameters generally reproduce our numerical light curves to within a factor of a few throughout our parameter space. However, the highest density/lowest energy light curve diverges from the power law fit at late times as the outflow enters into the deep Newtonian regime (see Sironi & Giannios 2013). Also, the 2D, $n_{18} = 60 \text{ cm}^{-3}$ light curve has a somewhat steeper late time light curve that declines as t^{-2} .

Fig. 7 compares the light curves for observers aligned with the jet axis (on-axis) with those at an angle of 0.8 radians from the jet axis (off-axis). While the on- and off-axis light curves agree well for $n_{18} = 2000 \text{ cm}^{-3}$, the off-axis luminosity for $n_{18} = 2 \text{ cm}^{-3}$ is smaller by an order of magnitude at peak. This is because the peak of the on-axis light curve is dominated by the fast component of the jet, which would not be visible for significantly off-axis observers. However, we find that the late time light curve is nearly independent of viewing angle.

The top panel of Fig. 8 shows 1D on-axis radio light curves for our fiducial gas density profile, $n \propto r^{-1}$, and a core galaxy profile (equation A1), both with $n_{18} = 2 \text{ cm}^{-3}$. The light curves differ by at most a factor of a few. The core and cusp light curves are even closer at higher densities, and virtually indistinguishable at $n_{18} = 2000 \text{ cm}^{-3}$. This is because for larger ambient densities, the jet only samples small radii, where the core and cusp profiles are similar (see Fig. 1). It is only at lower densities, for which the Sedov

radius lies outside of the flattening of the core density profile, that noticeable differences emerge.

The bottom panel of Fig. 8 compares the 1D on-axis light curves for $n \propto r^{-1}$ and $n \propto r^{-1.5}$ gas density profiles with $n_{18} = 60 \text{ cm}^{-3}$. For most times the light curves agree well, which is perhaps not surprising because the density in these two models agrees at 10^{18} cm , which is close to the Sedov radius for these density profiles. However, in 2D hydrodynamical simulations, a jet propagating through an $r^{-1.5}$ density profile develops a more prolate structure than a jet propagating through an r^{-1} profile. This results in a light curve with a much steeper late time slope (see dash-dotted line in Fig. 8), although we note that the peak luminosity is nearly the same for the $n \propto r^{-1}$ and $n \propto r^{-1.5}$ density profiles.

3.3.1 Reverse Shock Emission?

Our calculations shown in Figs. 4 and 6-8 include only emission from the forward shock (shocked CNM), while in principle the reverse shock (shocked jet) also contributes to the radio light curve.

The fraction of the initial kinetic energy of the jet which is dissipated by the reverse shock provides a first-order estimate of its maximum contribution to the radio light curve. Fig. 5 shows contours of the fraction of the kinetic energy of the slow component dissipated by the reverse shock as a function of the jet energy and CNM density, n_{18} . This is es-

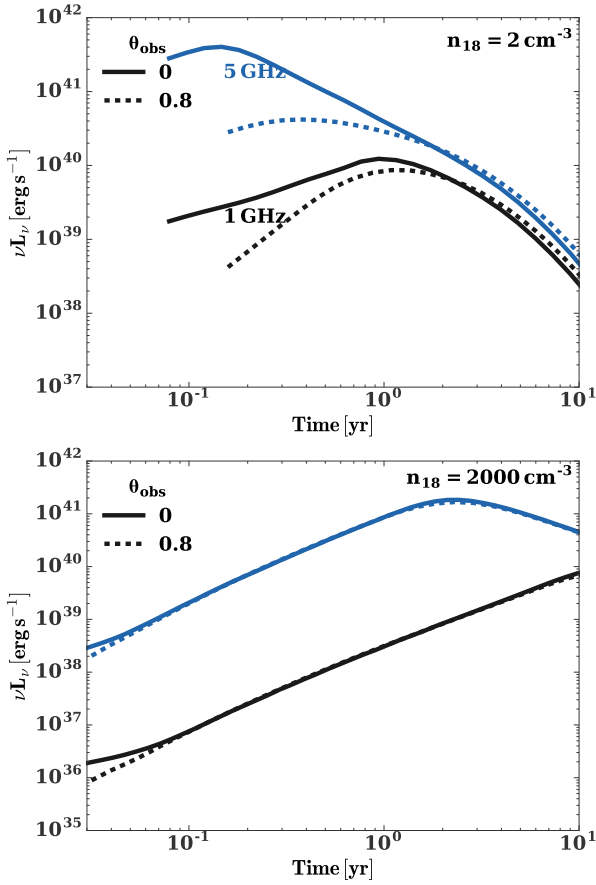


Figure 7. Comparison between on-axis (solid line) and off-axis (dashed line) light curves from our 1D simulations. The off-axis light curves are calculated for an observer viewing angle of $\theta_{\text{obs}}=0.8$. We adopt a density profile of $n \propto r^{-1}$. We note that the steepening of the $n_{18} = 2 \text{ cm}^{-3}$ light curves after 2 years is not physical and is due to limited angular resolution (see Mimica et al. 2016).

timated by integrating the shock evolution determined from the jump conditions (see Appendix C for details), approximating the jet as a constant source of duration $t_0 = 5 \times 10^5 \text{ s}$ and Lorentz factor $\Gamma = 2$. The parameters defining our grid of numerical solutions are shown in Fig. 5 as red squares.

Fig. 5 shows that for high ambient densities and/or low energy jets, the reverse shock dissipates an order unity fraction of the kinetic energy of the jet. Even for our highest energy/lowest density model ($n_{18} = 2 \text{ cm}^{-3}$ and $E_j = 5 \times 10^{53} \text{ erg}$) the reverse shock will dissipate of order 20% of the jet energy. Fig. 9 shows the 5 GHz and 30 GHz light curve for this case, separated into contributions from the forward and reverse shocks. The reverse shock emission is comparable to that from the forward shock for the first month. However, this overstates the true contribution of the reverse shock to the observed emission because the latter is strongly attenuated by absorption from the front of the jet, which has not been included in the reverse shock light curve in Fig. 9. For 5 GHz the contribution of the reverse shock to the total light curve is negligible at all times. For the 30 GHz, the peak luminosity increases by a factor of 1.5 after reverse shock emission is taken into account. While the reverse shock dissipates an even larger fraction of the jet energy for higher

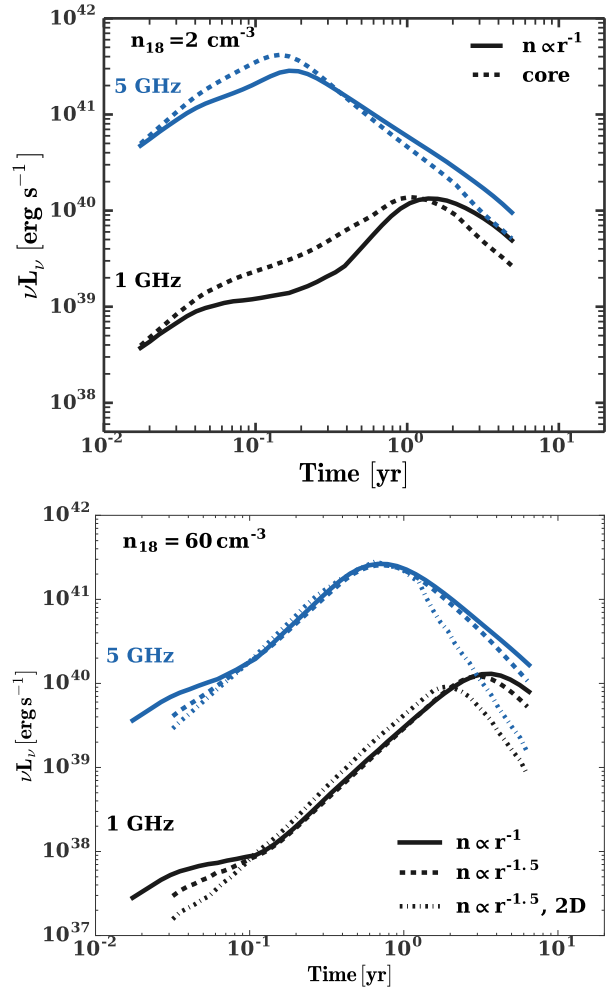


Figure 8. *Top:* Comparison between on-axis light curves for our fiducial $n \propto r^{-1}$ gas density profile, corresponding to a cusp-like galaxy, and the core galaxy profile defined by (A1) with $r_s = 10^{18} \text{ cm}$. *Bottom:* Comparison between on-axis light curves calculated from 1D simulations with $n \propto r^{-1}$ (solid) and $n \propto r^{-1.5}$ (dashed) gas density profiles. The dash-dotted line shows the on-axis light curve for a 2D simulation with an $n \propto r^{-1.5}$ gas density profile.

ambient density, its emission will be even more heavily absorbed. We conclude that the reverse shock emission can be neglected for the high energy jets with $E \gtrsim 10^{53} \text{ erg}$, consistent with the reverse shock not contributing appreciably to SwJ1644 (Metzger et al. 2012).

For low energy jets, we find that the jet is crushed at early times, even for low values of n_{18} . In the case of very low power jets the reverse shock structure is replaced by a number of recollimation shocks (similar to the structure seen in e.g. Mimica et al. 2009b). While this is potentially a very interesting case since the emitting volume from recollimation shocks can be larger than from a single reverse shock, because of a much more complex structure we defer a more detailed study of the emission from the reverse/recollimation shocks in the the low energy case to future work.

As a final note of caution, even if the reverse shock dissipates most of the bulk kinetic energy into thermal energy, the latter can be converted back to kinetic energy through adiabatic expansion. However, we expect that the

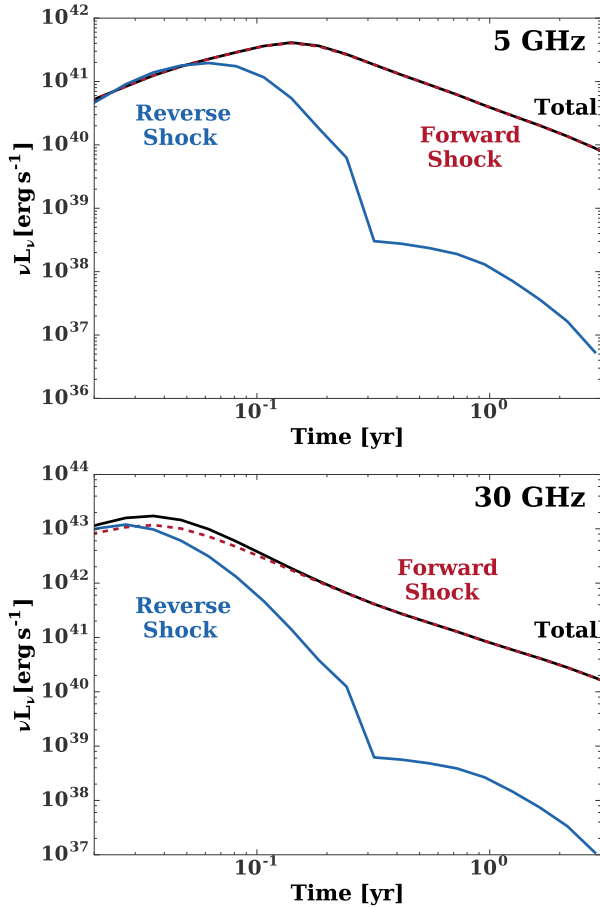


Figure 9. Radio light curve from the forward shock (red line), reverse shock (blue), and the total light curve (black) for a jet of energy 5×10^{53} erg and CNM density $n \propto r^{-1}$ with $n_{18} = 2$ cm^{-3} . The reverse shock light curve excludes absorption from the front of the jet, which when included in the full calculation results in large attenuation of the emission, such that the total light curve is dominated by the forward shock.

re-expansion will be relatively isotropic compared to the original jet, because the matter is first slowed to mildly relativistic speeds. The net result of an ultra-strong reverse shock (due to a weak jet, and/or an unusually high CNM density) is therefore likely to be the production of two quasi-spherical lobes on either side of the black hole, centered about the deceleration radius (Giannios & Metzger 2011).

3.4 Parameter Space of Jet-CNM Interaction

The left column of Fig. 10 shows contours of the peak luminosity (thick lines) as derived from our grid of numerical on-axis models, covering the parameter space of jet energy E and density n_{18} . Also shown with thin lines is the luminosity arising from just the slow, wide angle component. The fast, narrow component of the jet dominates at high frequencies and low densities, while the slow, wide component dominates for large n_{18} and low frequencies. Remarkably, the total peak luminosity is nearly independent of the ambient gas density; this is in part coincidental, as the fast and slow peak fluxes individually vary across the parameter space. For off-axis jets, the peak luminosity is dominated

by just that of the slow component, and thus would be a decreasing function of the ambient density above 1 GHz.

The right column of Fig. 10 compares our numerical results for the slow component to the analytic estimate given in equation (18). For large n_{18} , the optically thick case reproduces the peak luminosity to within a factor of a few. By contrast, for 30 GHz and low n_{18} , the numerical results are closer to the optically thin limit.

The left column of Fig. 11 shows contours of the time of peak flux in days, separately for the slow component (thin lines) and the total light curve (thick lines). Shown for comparison in the panels in the right column is the peak time as estimated from equation (19). At 30 GHz, the peak time decreases with n_{18} at small values of the latter, because in this regime the jet is optically thin prior to the deceleration time.

3.4.1 Comparison with radio detections and upper limits.

Fig. 6 compares our fiducial 5×10^{53} erg on-axis jet model to radio detections and upper limits derived from follow-up observations of TDE flares (including SwJ1644¹⁰), as compiled in Table 2. All of the 5 GHz light curves, corresponding CNM densities, n_{18} , of 2, 60, and 2000 cm^{-3} , fall above the upper limits. In agreement with the results of previous work, we conclude that most TDEs discovered by their optical/UV or soft X-ray emission do not produce jets as powerful as that responsible for SwJ1644 (Bower et al. 2013; van Velzen et al. 2013; Mimica et al. 2015), a result which is now found to hold for a broad range of CNM environments.

The peak radio luminosity at frequencies $\lesssim 1$ GHz is weakly dependent on the ambient gas density. Radio observations conducted from several months to years after a tidal disruption flare, which tightly constrain the peak flux of a putative jet, can therefore be used to constrain the jet energy. Equation (18) shows that an upper limit of F_{ul} on the flux density at 1 GHz of a source at distance d_L results in an upper limit on the jet energy of

$$E \lesssim 4.3 \times 10^{49} \left(\frac{F_{\text{ul}}}{50 \mu\text{Jy}} \right)^{1.1} \left(\frac{d_L}{200 \text{ Mpc}} \right)^{2.3} \text{ erg}, \quad (21)$$

where we have taken $n_{18} = 2000 \text{ cm}^{-3}$ (but the constraint is not overly sensitive to this choice for $n_{18} \geq 2 \text{ cm}^{-3}$)¹¹. Radio measurements of the peak flux following a TDE therefore serve as calorimeters of the total energy released in a relativistic jet (or spherical outflow).

If the peak flux is missed, late time measurements can still be used to constrain the jet energy. In fact, with late time measurements it is possible to place constraints on the energy of the jet/outflow using higher frequency radio data. Fig. 12 compares our analytic fit to the on-axis 5 GHz synchrotron light curve (eq. 20) for different jet energies and existing radio upper limits for $n_{18} = 10 \text{ cm}^{-3}$, the minimum expected density for stellar populations observed in TDE

¹⁰ Detailed comparison of our model with radio data from SwJ1644 data is given in Mimica et al. 2015.

¹¹ The peak luminosity will decrease approximately linearly with n_{18} for $n_{18} \leq 2 \text{ cm}^{-3}$. For the smallest plausible value of n_{18} , 0.3 cm^{-3} , the normalization in equation (21) would increase by a factor of 7.

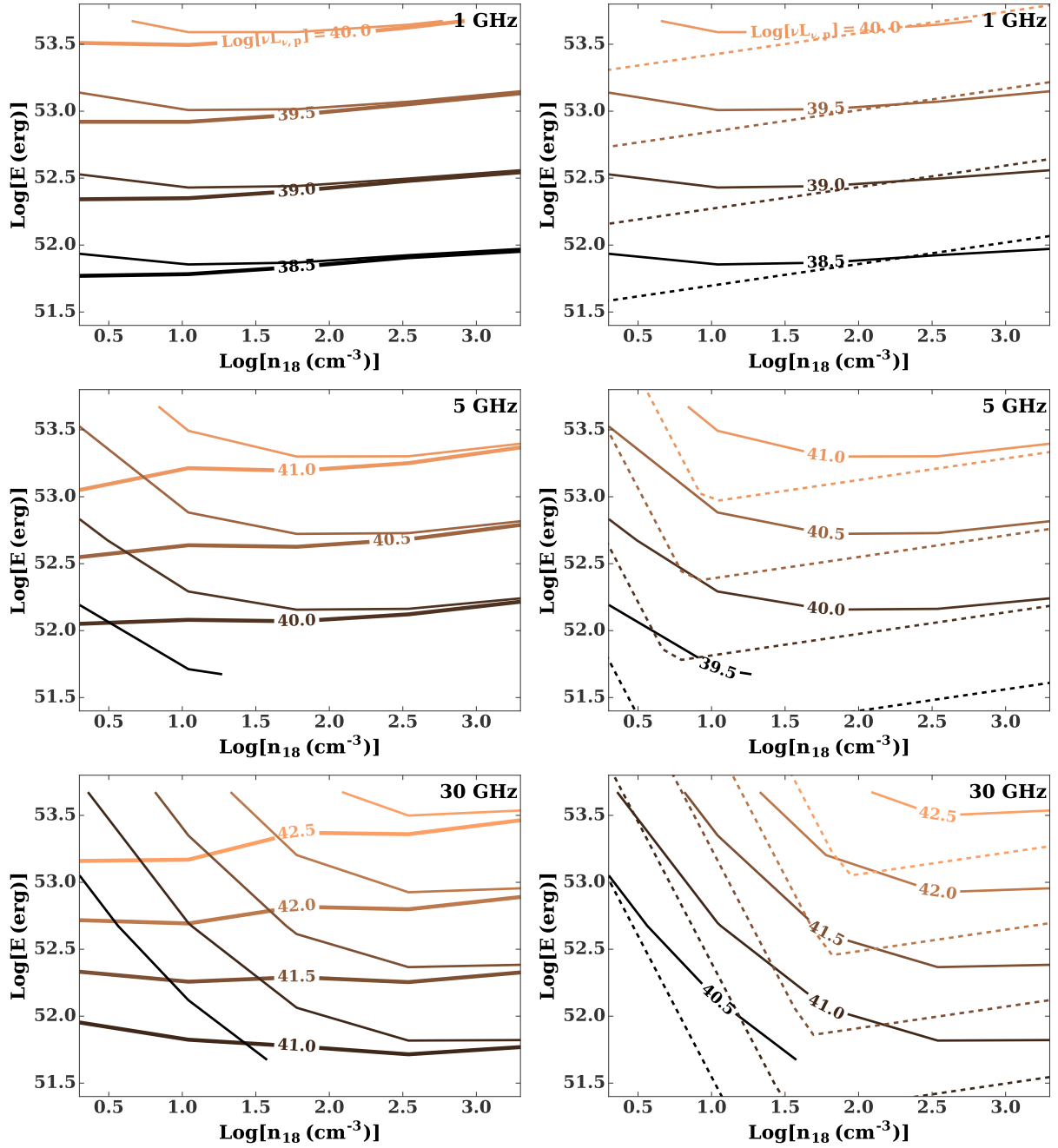


Figure 10. *Left:* Thick lines show the peak radio luminosity in the parameter space of jet energy and ambient gas density at 10^{18} cm, calculated from the grid of on-axis jet simulations in Table 1. Thin lines show contours of peak luminosity for the slow component light curve (§ 3.1). *Right:* Analytic estimate for the peak luminosity (dashed lines; eq. 18) compared to the numerical results for the slow component (solid lines).

host galaxies. An increase in n_{18} would simply shift the light curves to the right. Thus, for times after peak each light curve in Fig. 12 gives smallest plausible radio luminosity for the corresponding jet energy. As the upper limits are all taken at late times, the $n_{18}=10$ cm $^{-3}$ light curve which passes through each upper limit corresponds to the maximum jet energy consistent with it. We note that that in this case, the deceleration radius is inside both the influence radius and the stagnation radius, and thus we would expect the density profile there to be closer to $r^{-1.5}$, rather than

r^{-1} . A steeper density profile would cause a steeper late time decline in the light curve, and would make the upper limits less constraining. However, the steeper profile would imply a larger density at n_{18} , which would compensate for this.

Fig. 13 shows a histogram of the maximum jet energies consistent with the existing radio upper limits and detections of TDE flares with radio follow-up (see also Table 2). The detected events include ASSASN-14li, SwJ1644, and SwJ2058. For ASSASN-14li and SwJ1644 the lightcurves are well sampled, and the energy of the jet is relatively well

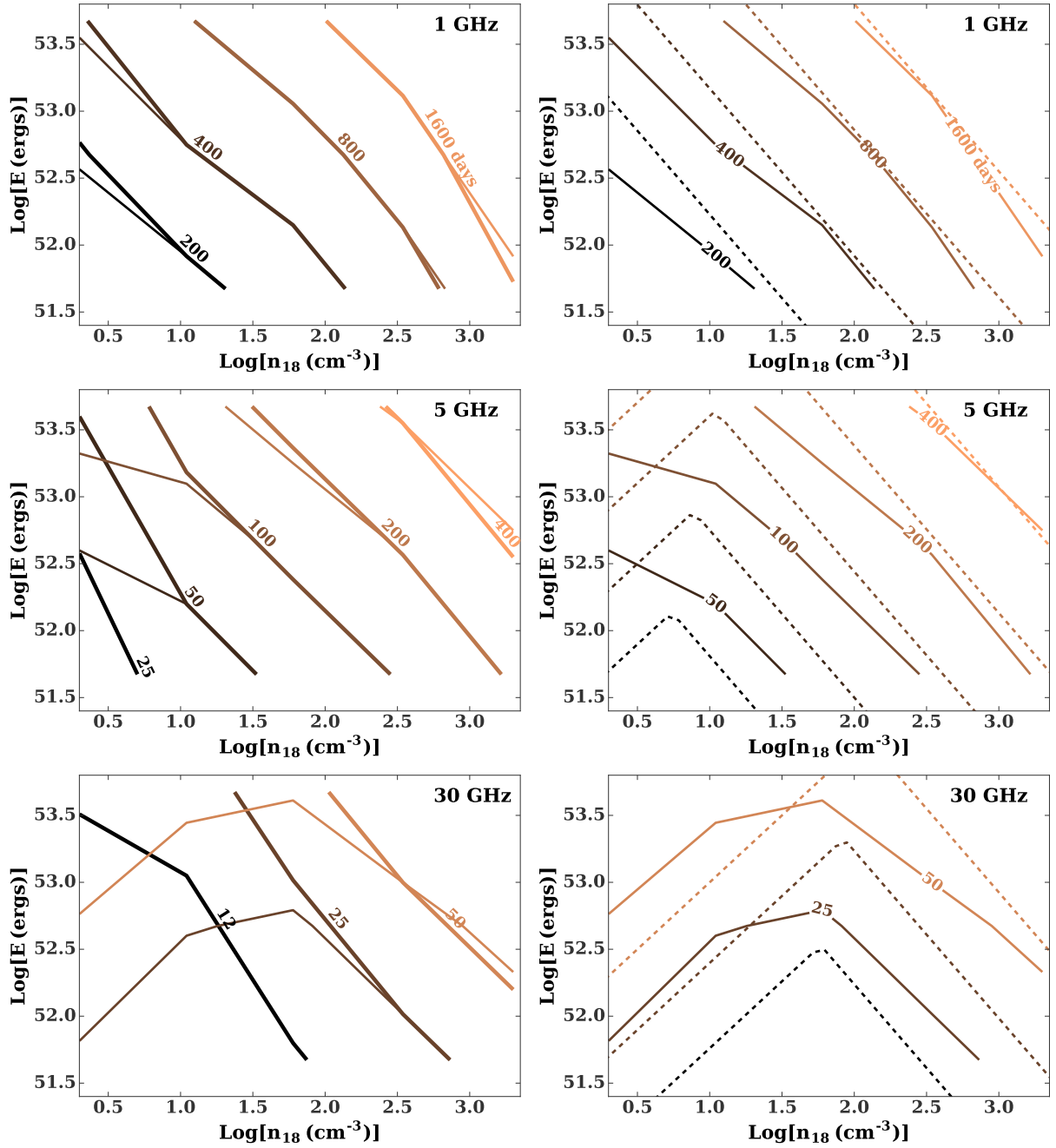


Figure 11. *Left:* Thick lines show peak time in days in the parameter space of jet energy and ambient gas density at 10^{18} cm, calculated from the grid of on-axis jet simulations in Table 1. Thin lines show contours of peak time for the slow component light curve (see 3.1). *Right:* Analytic scaling for the peak time (*dashed*, see equation 19) compared to the numerical results for the slow component (*solid*)

constrained to be $\approx 10^{48} - 10^{49}$ erg for ASSASN-14li (van Velzen et al. 2016; Alexander et al. 2016) and 5×10^{53} erg for SwJ1644 (Mimica et al. 2015). For SwJ2058, we take the jet energy to be 5×10^{53} erg, the same as its “twin” SwJ1644 (Cenko et al. 2012; Pasham et al. 2015).

4 SUMMARY AND CONCLUSIONS

We calculate the radio emission from tidal disruption event jets propagating through a range of plausible circumnuclear

gas densities. The latter are motivated by analytic estimates of the gas supply from stellar winds based on our previous work in GSM15. We simulate the jet propagation using both 1D and 2D hydrodynamic simulations, which we then post-process using a radiative transfer calculation to produce synchrotron light curves. To isolate the effects of the density profile and jet energy we employ a fixed two component jet model from Mimica et al. (2015), which produces an acceptable fit to the observed radio data of the on-axis jetted TDE SwJ1644. Our conclusions are summarized as follows.

Table 2. Inferred jet/outflow energies (and bounds) from radio detections and upper limits of optical/UV and soft X-ray TDE candidates. For each event detected in the radio there are multiple observations at different times/frequencies. Thus, we leave a dash in the time frequency, and luminosity columns and simply refer to reference in column “Ref.”

Source	D_L (Mpc)	t (yr)	ν (GHz)	νL_ν (10^{36} erg s $^{-1}$)	Ref.	Energy (erg)
Detections						
ASSASN-14li	93	-	-	-	1	$10^{48} - 10^{49}$
SwJ1644	1900	-	-	-	2	5×10^{53}
SwJ2058	8400	-	-	-	3	5×10^{53}
Upper limits						
RXJ1624+7554	290	21.67	3.0	27	4	$< 1.4 \times 10^{53}$
RXJ1242-1119	230	19.89	3.0	17	4	$< 9.6 \times 10^{52}$
SDSSJ1323+48	410	8.61	3.0	100	4	$< 1.0 \times 10^{53}$
SDSSJ1311-01	900	8.21	3.0	280	4	$< 1.9 \times 10^{53}$
D1-9	1800	8.0	5.0	840	5	$< 4.1 \times 10^{53}$
TDE1	660	5.4	5.0	130	5	$< 7.1 \times 10^{52}$
D23H-1	930	4.8	5.0	210	5	$< 8.2 \times 10^{52}$
PTF10iya	1100	1.6	5.0	320	5	$< 2.5 \times 10^{52}$
PS1-10jh	840	0.71	5.0	320	5	$< 8.7 \times 10^{51}$
NGC5905	49	21.91	3.0	1.7	4	$< 2.4 \times 10^{52}$
NGC5905	49	6.0	8.6	3.7	6	$< 8.2 \times 10^{51}$
D3-13	2000	7.6	5.0	1000	5	$< 4.3 \times 10^{53}$
D3-13	2000	1.8	1.4	1000	7	$< 2.5 \times 10^{53}$
TDE2	1300	4.3	5.0	610	5	$< 1.4 \times 10^{53}$
TDE2	1300	1.1	8.4	1700	8	$< 5.0 \times 10^{52}$
SDSSJ1201+30	710	1.4	7.9	1100	9	$< 5.0 \times 10^{52}$
PTF09axc	550	5.0	3.5	700	10	$< 1.8 \times 10^{53}$
PTF09axc	550	5.0	6.1	550	10	$< 1.7 \times 10^{53}$

References: (1) Alexander et al. (2016); van Velzen et al. (2016), (2) Berger et al. (2012); Zauderer et al. (2013); Yang et al. (2016) (3) Cenko et al. (2012), (4) Bower et al. (2013), (5) van Velzen et al. (2013), (6) Bade et al. (1996); Komossa & Dahlem (2001), (7) Gezari et al. (2008); Bower (2011b), (8) van Velzen et al. (2011), (9) Saxton et al. (2012), (10) Arcavi et al. (2014). All upper limits are 5σ . Luminosity distances are calculated using the identified host galaxy redshift and the best fitting Planck 2013 cosmology ($\Omega_M = 0.307$ and $H_0 = 67.8$ km s $^{-1}$ Mpc $^{-1}$), as implemented in the Astropy cosmology package.

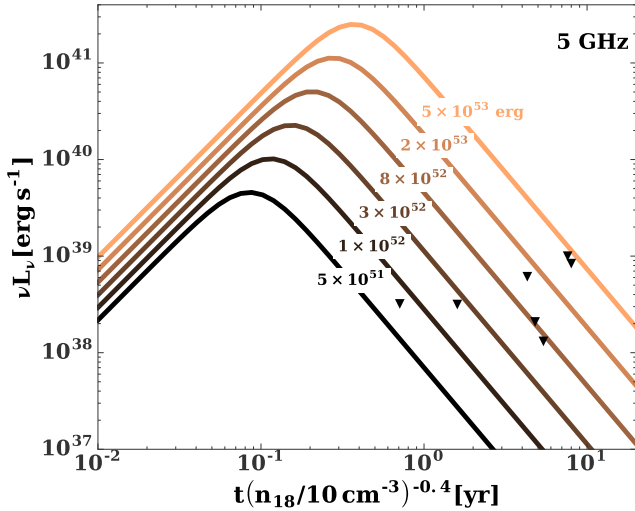


Figure 12. Upper limits and 5 GHz analytic light curves (eqn. 20 with $s = 1$, $a_1 = 1.7$, and $a_2 = -2$) for different jet energies. We use the peak time and luminosity from our numerical $n_{18}=11$ cm $^{-3}$ light curve for the highest energy light curve, as our analytic fits (eqns. 18 and 19) underestimate the peak luminosity a factor of ~ 2 for this density. Then we use our analytic results to scale this light curve to lower energies.

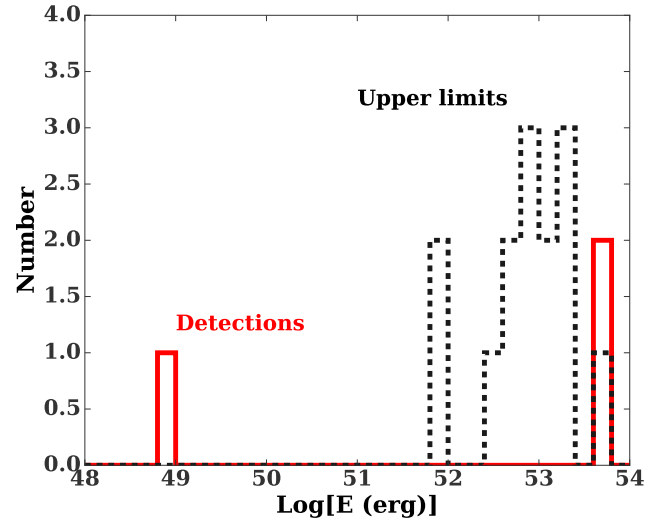


Figure 13. Histogram of jet energies consistent with existing radio detections (ASSASN-14li, SwJ1644, and SwJ2058) and upper limits (Table 1 of Mimica et al. 2015 and Arcavi et al. 2014), as summarized in Table 2.

(i) The radio emission is most sensitive to the density at the jet deceleration radius, which is typically $r_{\text{dec}} \sim 0.1 - 1$

pc (Fig. 1). We estimate the radial profile of nuclear gas densities expected from injection of stellar wind material for different star formation histories, and find that the gas density at 10^{18} cm lies in the range $n_{18} \sim 0.3M_{\bullet,7}^{-0.4} - 1,300M_{\bullet,7}^{0.5}$ cm^{-3} , with $n_{18} \sim 10 \text{ cm}^{-3}$ for star formation histories typical of TDE host galaxies (excluding a possible factor of ~ 2 reduction from mass drop out from star formation).

(ii) The slope of the CNM gas density profile depends on the slope of the stellar density profile. A TDE host galaxy likely possesses a cuspy stellar density profile inside of a few pc, with $\rho_{\star} \propto r^{-1.7}$. This translates into a gas density profile ranging from $n \propto r^{-0.7}$ on large scales to $n \propto r^{-1.5}$ on very small scales, well inside the stagnation radius, r_s and influence radius r_{inf} . In general, we expect a density profile bracketed by $n \propto r^{-0.7}$ and $n \propto r^{-1.5}$ near the Sedov/deceleration radius. For simplicity we adopt a single power law $n \propto r^{-1}$ as our fiducial density profile.

(iii) We perform hydrodynamical simulations of our two component jet model for a range of plausible density profiles and normalizations $n_{18} = 2, 11, 60, 345, \text{ or } 2000 \text{ cm}^{-3}$. We find bright radio emission at a few GHz across this entire range of densities. The peak luminosity is only weakly dependent on the chosen density profile for on-axis jets. For off-axis jets, the peak luminosity at 1 GHz is insensitive to the CNM density profile and viewing angle for $n_{18} \geq 2 \text{ cm}^{-3}$, although it will be a stronger function of density at higher frequencies. While the peak radio flux is largely insensitive to the radial power-law slope for fixed n_{18} , a steeper profile $n \propto r^{-1.5}$ (e.g., as expected at radii $\ll r_s, r_{\text{inf}}$) alters the 2D dynamical evolution of the jet in a non-trivial way, resulting in a steeper post maximum decline of the radio light curve.

(iv) The time of the peak radio luminosity depends more sensitively on the density and can be as early as months, or as late as one decade, after the TDE. By comparing our calculated light curves with upper limits from a set of optical/UV and soft X-ray selected TDE, we show that most of these sources cannot have jets as powerful as SwJ1644.

(v) In general, we only calculate the synchrotron radio emission from the forward shock, and neglect reverse shock emission. For high energy jets ($E \gtrsim 10^{53}$ erg), and frequencies $\lesssim 30$ GHz, we find that the reverse shock has minimal impact on the total light curve. For low energy jets the reverse shock structure may be replaced by a series of recollimation shocks with a large emitting volume, which could contribute significantly to the total emission.

Prompt radio follow-up, as well as regular monitoring, of future TDE flares would provide tighter constraints on the presence of jets. Radio afterglows can serve as calorimeters for off-axis jets launched by TDEs, and future observational efforts that capture the peak radio flux in thermally detected TDEs will add to the diversity of jet energies observed in TDE flares. The broad range of energies (both detections and upper limits) already seen in TDE jets presents an interesting puzzle for theoretical models of jet launching.

ACKNOWLEDGMENTS

We acknowledge helpful conversations with Jerry Ostriker, Luca Ciotti, James Guillochon, and Yue Shen. BDM and AG acknowledge support from the NSF (grant AST-1410950), NASA (grants NNX15AR47G, NNX15AU77G,

NNX16AB30G), the Alfred P. Sloan Foundation, and the Research Corporation for Science Advancement. NS acknowledges support from the NASA Einstein Postdoctoral Fellowship Program (grant SAO PF5-160145). DG acknowledges support from NASA through grant NNX16AB32G issued through the Astrophysics Theory Program and support from the Research Corporation for Science Advancements Scialog program. PM and MAA acknowledge financial support from the European Research Council (ERC) through the Starting Independent Researcher Grant CAMAP-259276, and the partial support of grants AYA2013-40979-P, AYA2015-66899-C2-1-P and PROMETEO-II-2014-069. We thankfully acknowledge the computer resources, technical expertise and assistance provided by the Servei de Informàtica of the University of Valencia and Columbia University's Yeti Computer Cluster. This research made use of Astropy, a community-developed core Python package for Astronomy (Astropy Collaboration, 2013).

APPENDIX A: CORE PROFILE

Fig. 8 compares the results of radio light curves from jets propagating in core and cusp like gas density profiles (Fig. 1). We use the following analytic expression to approximate the core galaxy CNM profile in Fig. 1

$$\begin{cases} n = n(r_s)k(x) & 0.4 \leq x \leq 2.0 \\ n = 2.0n(r_s)(x/0.4)^{-0.95} & x < 0.4 \\ n = 0.75n(r_s)(x/2.0)^{-0.26} & x > 2, \end{cases} \quad (\text{A1})$$

where

$$x = r/r_s \quad (\text{A2})$$

$$k(x) = \frac{45}{19} \frac{1}{x^{3/2}} \frac{1 - x^{1.9}}{9 - 19x \frac{x^{0.9} - 1}{x^{1.9} - 1}}$$

To isolate the effects of the shape of the density profile, we consider a core density profile with a stagnation radius $r_s = 10^{18}$ cm and density normalization $n_{18} = 2000 \text{ cm}^{-3}$ which match those of our high density cusp model.

APPENDIX B: PEAK LUMINOSITIES AND TIMES

Leventis et al. (2012) present analytic scaling relations for the synchrotron flux of a spherical blast wave propagating through a medium with a power law density profile, $n \propto r^{-k}$. Here we make use of their results to estimate the peak radio flux of the slow (sheath) component of the jet.

During the late-time, Newtonian stage of the jet evolution, synchrotron self absorption is important for frequencies below

$$\nu_{\text{sa}} = C_1(p, k) E_{54}^{\frac{10p - kp - 6k}{2(4+p)(5-k)}} n_{18}^{\frac{30-5p}{2(4+p)(5-k)}} \epsilon_e^{\frac{2(p-1)}{4+p}} \epsilon_b^{\frac{p+2}{2(4+p)}} t^{\frac{10-8k-15p+4kp}{(4+p)(5-k)}}, \quad (\text{B1})$$

where $E = 10^{54} E_{54}$ erg is the blast wave energy and $C_1(p, k)$ is a normalization factor. Equation (B1) is valid only if self-absorption frequency is greater than the synchrotron peak frequency,

$$\nu_m = C_2(p, k) E_{54}^{\frac{10-k}{2(5-k)}} n_{18}^{-\frac{5}{2(5-k)}} \epsilon_e^2 \epsilon_b^{1/2} t^{\frac{4k-15}{5-k}}. \quad (\text{B2})$$

The light curve will peak at the deceleration time (eq. 4) in case the emitting region is optically thin then. Otherwise, it will occur after the deceleration time, when the self-absorption frequency crosses through the observing band. The peak time for these two cases is

$$t_p \approx \begin{cases} 0.5 (50(3-k) E_{54})^{1/(3-k)} \\ \times \Gamma^{(2k-8)/(3-k)} n_{18}^{-1/(3-k)} \text{ yr} & \text{Opt. Thin} \\ C_1(p, k)^{-\frac{(5-k)(4+p)}{10-8k-15p+4kp}} E_{54}^{-\frac{-kp-6k+10p}{2(4kp-8k-15p+10)}} \\ \times n_{18}^{-\frac{30-5p}{2(4kp-8k-15p+10)}} \nu_{\text{obs}}^{\frac{(5-k)(p+4)}{4kp-8k-15p+10}} \\ \times \epsilon_b^{-\frac{(5-k)(p+2)}{2(4kp-8k-15p+10)}} \epsilon_e^{-\frac{2(5-k)(p-1)}{4kp-8k-15p+10}} & \text{Opt. Thick,} \end{cases} \quad (\text{B3})$$

where Γ is the initial jet Lorentz factor.

The unabsorbed flux at the peak frequency is given by

$$F_{\nu_m} = C_3(p, k) E_{54}^{\frac{8-3k}{2(5-k)}} n_{18}^{\frac{7}{2(5-k)}} \epsilon_b^{1/2} t^{\frac{3-2k}{5-k}} \quad (\text{B4})$$

Extrapolating to the observer frequency gives

$$\nu_{\text{obs}} F_p(\nu_{\text{obs}}) = \nu_{\text{obs}} F_{\nu_m} \left(\frac{\nu_{\text{obs}}}{\nu_m} \right)^{-(p-1)/2}. \quad (\text{B5})$$

Combining equations (B2), (B3), (B4), and (B5), we find

$$\nu_{\text{obs}} F_p(\nu_{\text{obs}}) \propto \begin{cases} E_{54}^{\frac{k(p+5)-12}{4(k-3)}} n_{18}^{-\frac{3(p+1)}{4(k-3)}} \nu_{\text{obs}}^{\frac{3-p}{2}} \epsilon_b^{\frac{p+1}{4}} \epsilon_e^{p-1} & \text{Opt. Thin} \\ E_{54}^{\frac{k(-(p-2))-10p+3}{4k(p-2)-15p+10}} \\ \times n_{18}^{\frac{11(p-2)}{4k(p-2)-15p+10}} \nu_{\text{obs}}^{\frac{14k(p-2)-47p+57}{4k(p-2)-15p+10}} \\ \times \epsilon_b^{\frac{k(-(p-2))+p-8}{4k(p-2)-15p+10}} \epsilon_e^{-\frac{11(p-1)}{4k(p-2)-15p+10}} & \text{Opt. Thick} \end{cases} \quad (\text{B6})$$

After peak, we expect that the flux scales as

$$F_\nu \propto t^{\frac{21-8k-15p+4kp}{10-2k}}. \quad (\text{B7})$$

APPENDIX C: REVERSE SHOCK

Here we estimate the fraction of the kinetic energy of the jet that is dissipated by the reverse shock, as opposed to the forward shock whose contribution is the focus of this paper. From continuity, the comoving density of a relativistic jet is given by (e.g. Uhm & Beloborodov 2007)

$$n_j = \frac{L_{j,\text{iso}}}{4\pi r^2 \Gamma_j^2 c^3 m_p (1 + r\dot{\Gamma}_j/c\Gamma^3)} \approx \frac{L_{j,\text{iso}}}{4\pi r^2 \Gamma^2 c^3 m_p}, \quad (\text{C1})$$

where $L_{j,\text{iso}}$ is the isotropic equivalent luminosity. The second term in the denominator can be neglected if the jet Lorentz factor changes slowly ($\dot{\Gamma}_j \ll c\Gamma^3/r$), a condition which is satisfied at radii $r < r_{\text{dec}}$ if Γ changes slowly on a timescale $\gtrsim t_0$, where t_0 is the jet duration.

The common Lorentz factor of the shocked CNM and the shocked jet can be estimated using the relativistic shock

jump condition and pressure equality between the forward and reverse shocks. In the ultra-relativistic limit this gives,

$$\Gamma_{\text{sh}} \Big|_{\Gamma_{\text{sh}} \gg 1} = \Gamma \left[1 + 2\Gamma f^{-1/2} \right]^{-1/2}, \quad (\text{C2})$$

where

$$f \approx 40 L_{j,48} n_{18}^{-1} \Gamma_{10}^{-2} \left(\frac{r}{10^{18} \text{cm}} \right)^{-1} \quad (\text{C3})$$

is the ratio of the density of the jet to that of the CNM. Equation (C2) is inaccurate for mildly relativistic or non-relativistic flows, in which case we apply the more general expression for Γ_{sh} given by Beloborodov & Uhm (2006) (their eq. 3, see also Mimica & Aloy 2010)

$$\frac{\Gamma_{\text{sh}}^2 - 1}{\Gamma_{43}^2 - 1} f^{-1} = 1, \quad (\text{C4})$$

where

$$\Gamma_{43} = \Gamma \Gamma_{\text{sh}} (1 - \beta_{\text{sh}} \beta_j), \quad (\text{C5})$$

is the Lorentz of shocked jet in the frame of the unshocked jet. Combining equations (C4) and (C5), we obtain

$$\Gamma_{\text{sh}}(f) = \sqrt{\frac{f(\Gamma^2(f-3) - 2(\Gamma^2-1)\Gamma\sqrt{f} + 1) + 1}{(f+1)^2 - 4\Gamma^2 f}} \\ \Gamma_{43}(f) = \sqrt{\frac{4\Gamma f^{3/2} + f^2 + \Gamma^4 f + 4\Gamma^3 \sqrt{f} + 2\Gamma^2(2f+1) + f - 1}{(2\Gamma\sqrt{f} + f + 1)^2}} \quad (\text{C6})$$

In the lab frame the reverse shock moves with a velocity

$$\beta_{\text{rs}} = \frac{\beta_{\text{sh}}(f) - \beta_{43}(f)/3}{1 - \beta_{\text{sh}}(f)\beta_{43}(f)/3}. \quad (\text{C7})$$

Equations (C6) and (C7) can be used to determine the radius of the shocks when the reverse shock crosses the trailing edge of the jet and the value of $\Gamma_{\text{sh,rs}}$ at this time. This involves numerically integrating $\beta_{\text{rs}}/\beta_j = dr_{\text{rs}}/dr_{\text{ej}}$, where r_{rs} is the position of the reverse and r_{ej} is the position of the back of the jet. The latter allows us to calculate what fraction of the initial kinetic energy of the jet is dissipated at the reverse shock, instead of being transferred to the shocked external medium via the forward shock. This is approximately given by

$$f_{\text{ke}} \approx \frac{\Gamma - \Gamma_{\text{sh,rs}}}{\Gamma - 1} \quad (\text{C8})$$

REFERENCES

- Alexander K. D., Berger E., Guillochon J., Zauderer B. A., Williams P. K. G., 2016, *ApJ*, **819**, L25
- Araudo A. T., Bosch-Ramon V., Romero G. E., 2009, *A&A*, **503**, 673
- Arcavi I., et al., 2014, *ApJ*, **793**, 38
- Bade N., Komossa S., Dahlem M., 1996, *A&A*, **309**, L35
- Baganoff F. K., et al., 2003, *ApJ*, **591**, 891
- Bartko H., et al., 2010, *ApJ*, **708**, 834
- Becklin E. E., Gatley I., Werner M. W., 1982, *ApJ*, **258**, 135
- Beloborodov A. M., Uhm Z. L., 2006, *ApJ*, **651**, L1
- Berger E., Zauderer A., Pooley G. G., Soderberg A. M., Sari R., Brunthaler A., Bietenholz M. F., 2012, *ApJ*, **748**, 36
- Bloom J. S., et al., 2011, *Science*, **333**, 203
- Bonnerot C., Rossi E. M., Lodato G., Price D. J., 2016, *MNRAS*, **455**, 2253
- Bower G. C., 2011a, *ApJ*, **732**, L12
- Bower G. C., 2011b, *ApJ*, **732**, L12
- Bower G. C., Metzger B. D., Cenko S. B., Silverman J. M., Bloom J. S., 2013, *ApJ*, **763**, 84
- Brown G. C., Levan A. J., Stanway E. R., Tanvir N. R., Cenko S. B., Berger E., Chornock R., Cucchiaria A., 2015, *MNRAS*, **452**, 4297
- Burrows D. N., et al., 2011, *Nature*, **476**, 421
- Campana S., Mainetti D., Colpi M., Lodato G., D'Avanzo P., Evans P. A., Moretti A., 2015, *A&A*, **581**, A17
- Carter B., Luminet J. P., 1982, *Nature*, **296**, 211
- Cenko S. B., et al., 2012, *ApJ*, **753**, 77
- Choi E., Wiita P. J., Ryu D., 2007, *ApJ*, **655**, 769
- Chornock R., et al., 2014, *ApJ*, **780**, 44
- Crumley P., Lu W., Santana R., Hernández R. A., Kumar P., Markoff S., 2016, *MNRAS*, **460**, 396
- Cuadra J., Nayakshin S., Springel V., Di Matteo T., 2006, *MNRAS*, **366**, 358
- De Colle F., Guillochon J., Naiman J., Ramirez-Ruiz E., 2012, *ApJ*, **760**, 103
- Drake A. J., et al., 2011, *ApJ*, **735**, 106
- Esquej P., Saxton R. D., Freyberg M. J., Read A. M., Altieri B., Sanchez-Portal M., Hasinger G., 2007, *A&A*, **462**, L49
- Ferrière K., 2012, *A&A*, **540**, A50
- French K. D., Arcavi I., Zabludoff A., 2016a, preprint, ([arXiv:1609.04755](https://arxiv.org/abs/1609.04755))
- French K. D., Arcavi I., Zabludoff A., 2016b, *ApJ*, **818**, L21
- Generozov A., Stone N. C., Metzger B. D., 2015, *MNRAS*, **453**, 775
- Genzel R., et al., 2003, *ApJ*, **594**, 812
- Georgiev I. Y., Böker T., 2014, *MNRAS*, **441**, 3570
- Gezari S., et al., 2008, *ApJ*, **676**, 944
- Gezari S., et al., 2009, *ApJ*, **698**, 1367
- Gezari S., et al., 2012, *Nature*, **485**, 217
- Giannios D., Metzger B. D., 2011, *MNRAS*, **416**, 2102
- Granot J., Sari R., 2002, *ApJ*, **568**, 820
- Greene J. E., et al., 2010, *ApJ*, **721**, 26
- Greiner J., Schwarz R., Zharikov S., Orío M., 2000, *A&A*, **362**, L25
- Grupe D., Thomas H.-C., Leighly K. M., 1999, *A&A*, **350**, L31
- Guillochon J., Ramirez-Ruiz E., 2013, *ApJ*, **767**, 25
- Guillochon J., McCourt M., Chen X., Johnson M. D., Berger E., 2016, *ApJ*, **822**, 48
- Hascoët R., Beloborodov A. M., Daigne F., Mochkovitch R., 2014, *ApJ*, **782**, 5
- Hayasaki K., Stone N., Loeb A., 2013, *MNRAS*, **434**, 909
- Hayasaki K., Stone N., Loeb A., 2016, *MNRAS*, **461**, 3760
- Hills J. G., 1975, *Nature*, **254**, 295
- Holoien T. W.-S., et al., 2014, *MNRAS*, **445**, 3263
- Holoien T. W.-S., et al., 2016a, *MNRAS*, **455**, 2918
- Holoien T. W.-S., et al., 2016b, *MNRAS*, **463**, 3813
- Holzer T. E., Axford W. I., 1970, *ARA&A*, **8**, 31
- Kelley L. Z., Tchekhovskoy A., Narayan R., 2014, *MNRAS*, **445**, 3919
- Kochanek C. S., 1994, *ApJ*, **422**, 508
- Komossa S., Dahlem M., 2001, ArXiv Astrophysics e-prints,
- Komossa S., Greiner J., 1999, *A&A*, **349**, L45
- Kormendy J., Ho L. C., 2013, *ARA&A*, **51**, 511
- Krolik J., Piran T., Svirski G., Cheng R. M., 2016, *ApJ*, **827**, 127
- Kumar P., Barniol Duran R., Bošnjak Ž., Piran T., 2013, *MNRAS*, **434**, 3078
- Lau R. M., Herter T. L., Morris M. R., Becklin E. E., Adams J. D., 2013, *ApJ*, **775**, 37
- Lauer T. R., et al., 2007, *ApJ*, **662**, 808
- Levan A. J., et al., 2011, *Science*, **333**, 199
- Leventis K., van Eerten H. J., Meliani Z., Wijers R. A. M. J., 2012, *MNRAS*, **427**, 1329
- Lu J. R., Do T., Ghez A. M., Morris M. R., Yelda S., Matthews K., 2013, *ApJ*, **764**, 155
- Maksym W. P., Ulmer M. P., Eracleous M., 2010, *ApJ*, **722**, 1035
- McConnell N. J., Ma C.-P., Gebhardt K., Wright S. A., Murphy J. D., Lauer T. R., Graham J. R., Richstone D. O., 2011, *Nature*, **480**, 215
- McCourt M., Sharma P., Quataert E., Parrish I. J., 2012, *MNRAS*, **419**, 3319
- Metzger B. D., Stone N. C., 2016, *MNRAS*, **461**, 948
- Metzger B. D., Giannios D., Mimica P., 2012, *MNRAS*, **420**, 3528
- Mimica P., Aloy M. A., 2010, *MNRAS*, **401**, 525
- Mimica P., Giannios D., 2011, *MNRAS*, **418**, 583
- Mimica P., Giannios D., Aloy M. A., 2009a, *A&A*, **494**, 879
- Mimica P., Aloy M.-A., Agudo I., Martí J. M., Gómez J. L., Miralles J. A., 2009b, *ApJ*, **696**, 1142
- Mimica P., Giannios D., Metzger B. D., Aloy M. A., 2015, *MNRAS*, **450**, 2824
- Mimica P., Aloy M. A., Giannios D., Metzger B. D., 2016, *Journal of Physics Conference Series*, **719**, 012008
- Nakar E., Granot J., 2007, *MNRAS*, **380**, 1744
- Obergaulinger M., Chimeno J., Mimica P., Aloy M., Iyudin A., 2015, *High Energy Density Physics*, **17**, Part A, 92
- Parfrey K., Giannios D., Beloborodov A. M., 2015, *MNRAS*, **446**, L61
- Pasham D. R., et al., 2015, *ApJ*, **805**, 68
- Perucho M., Bosch-Ramon V., 2012, *A&A*, **539**, A57
- Pfuhl O., et al., 2011, *ApJ*, **741**, 108
- Pracy M. B., Owers M. S., Couch W. J., Kuntschner H., Bekki K., Briggs F., Lah P., Zwaan M., 2012, *MNRAS*, **420**, 2232
- Quataert E., 2004, *ApJ*, **613**, 322
- Rees M. J., 1988, *Nature*, **333**, 523
- Sari R., Piran T., Narayan R., 1998, *ApJ*, **497**, L17
- Saxton R. D., Read A. M., Esquej P., Komossa S., Dougherty S., Rodriguez-Pascual P., Barrado D., 2012, *A&A*, **541**, A106
- Shiokawa H., Krolik J. H., Cheng R. M., Piran T., Noble S. C., 2015, *ApJ*, **804**, 85
- Sironi L., Giannios D., 2013, *ApJ*, **778**, 107
- Stone N., Loeb A., 2012, *Physical Review Letters*, **108**, 061302
- Stone N. C., Metzger B. D., 2016, *MNRAS*, **455**, 859
- Tchekhovskoy A., Metzger B. D., Giannios D., Kelley L. Z., 2014, *MNRAS*, **437**, 2744
- Uhm Z. L., Beloborodov A. M., 2007, *ApJ*, **665**, L93
- Vinkó J., et al., 2015, *ApJ*, **798**, 12
- Voss R., Diehl R., Hartmann D. H., Cerviño M., Vink J. S., Meynet G., Limongi M., Chieffi A., 2009, *A&A*, **504**, 531
- Wang J., Merritt D., 2004, *ApJ*, **600**, 149
- Wang Z., Wiita P. J., Hooda J. S., 2000, *ApJ*, **534**, 201
- Yang J., Paragi Z., van der Horst A. J., Gurvits L. I., Campbell R. M., Giannios D., An T., Komossa S., 2016, *MNRAS*, **462**, L66
- Zauderer B. A., et al., 2011, *Nature*, **476**, 425
- Zauderer B. A., Berger E., Margutti R., Pooley G. G., Sari R.,

- Soderberg A. M., Brunthaler A., Bietenholz M. F., 2013, [ApJ](#), **767**, 152
- van Eerten H. J., Meliani Z., Wijers R. A. M. J., Keppens R., 2009, [MNRAS](#), **398**, L63
- van Velzen S., et al., 2011, [ApJ](#), **741**, 73
- van Velzen S., Frail D. A., Körding E., Falcke H., 2013, [A&A](#), **552**, A5
- van Velzen S., et al., 2016, [Science](#), **351**, 62